

## RESEARCH ARTICLE

## Interactions of nuclear transport factors and surface-conjugated FG nucleoporins: Insights and limitations

Ryo Hayama<sup>1</sup>, Mirco Sorci<sup>2</sup>, John J. Keating IV<sup>2</sup>, Lee M. Hecht<sup>1</sup>, Joel L. Plawsky<sup>2</sup>, Georges Belfort<sup>2\*</sup>, Brian T. Chait<sup>3\*</sup>, Michael P. Rout<sup>1\*</sup>

**1** Laboratory of Cellular and Structural Biology, the Rockefeller University, New York, NY, United States of America, **2** Department of Chemical and Biological Engineering and Center for Biotechnology and Interdisciplinary Studies, Rensselaer Polytechnic Institute, Troy, NY, United States of America, **3** Laboratory of Mass Spectrometry and Gaseous Chemistry, the Rockefeller University, New York, NY, United States of America

☯ These authors contributed equally to this work.

\* [belfog@rpi.edu](mailto:belfog@rpi.edu) (GB); [chait@mail.rockefeller.edu](mailto:chait@mail.rockefeller.edu) (BTC); [rout@mail.rockefeller.edu](mailto:rout@mail.rockefeller.edu) (MPR)



## OPEN ACCESS

**Citation:** Hayama R, Sorci M, Keating IV JJ, Hecht LM, Plawsky JL, Belfort G, et al. (2019) Interactions of nuclear transport factors and surface-conjugated FG nucleoporins: Insights and limitations. PLoS ONE 14(6): e0217897. <https://doi.org/10.1371/journal.pone.0217897>

**Editor:** Bostjan Kobe, University of Queensland, AUSTRALIA

**Received:** March 28, 2019

**Accepted:** May 21, 2019

**Published:** June 6, 2019

**Copyright:** © 2019 Hayama et al. This is an open access article distributed under the terms of the [Creative Commons Attribution License](https://creativecommons.org/licenses/by/4.0/), which permits unrestricted use, distribution, and reproduction in any medium, provided the original author and source are credited.

**Data Availability Statement:** All relevant data are within the manuscript and its Supporting Information files.

**Funding:** This work was supported by: BTC, MPR: NIH P41GM109824; MPR: NIH R01GM112108; MPR: NIH R01GM117212. The funders had no role in study design, data collection and analysis, decision to publish, or preparation of the manuscript.

**Competing interests:** The authors have declared that no competing interests exist.

## Abstract

Protein-protein interactions are central to biological processes. *In vitro* methods to examine protein-protein interactions are generally categorized into two classes: in-solution and surface-based methods. Here, using the multivalent interactions between nucleocytoplasmic transport factors and intrinsically disordered FG repeat containing nuclear pore complex proteins as a model system, we examined the utility of three surface-based methods: atomic force microscopy, quartz crystal microbalance with dissipation, and surface plasmon resonance. Although results were comparable to those of previous reports, the apparent effect of mass transport limitations was demonstrated. Additional experiments with a loss-of-interaction FG repeat mutant variant demonstrated that the binding events that take place on surfaces can be unexpectedly complex, suggesting particular care must be exercised in interpretation of such data.

## Introduction

Protein-protein interactions are at the core of any biological system and regulate essential cellular functions; measuring their characteristics, such as stoichiometry, affinity and kinetics, is crucial for understanding their biological roles. There are multiple *in vitro* methods to characterize protein-protein interactions, among the most popular of which are surface-based such as enzyme-linked immunosorbent assay (ELISA) and surface plasmon resonance (SPR). These surface-based methods have been applied to a wide range of protein-protein interactions, from well-defined antigen-antibody interactions to those involving intrinsically disordered proteins (IDPs), a major class of proteins involved in various functions, many of whose detailed behaviors are still being characterized [1, 2]. Here, we examined the applicability of select surface-based techniques to the characterization of a complex system involving IDPs, specifically the

ones involved in the nucleocytoplasmic transport mediated by nuclear pore complexes (NPCs) [3–6].

NPCs are the sole conduits across the nuclear envelope; macromolecular exchange between the nucleoplasm and the cytoplasm occurs in their central tube, which is lined with extensive regions of intrinsically disordered FG nucleoporins (FG Nups), so-called because each carries multiple phenylalanine-glycine (FG) repeat motifs. It is generally agreed that protein-protein interactions between the FG repeat motifs in FG Nups and cargo-carrying transport factors (TFs) are central to selective and rapid nucleocytoplasmic transport across the NPC [4, 7]; however, the exact physical mechanisms of this transport have not been fully characterized. There have been many reports on measurements of the strengths and modes of interactions between FG Nups and TFs [8–19]. The methods employed to study the FG-TF interaction vary, although most of them utilize surface-based systems, including microtiter plate and beads binding assays [8–12, 20], atomic force microscopy (AFM) [21–23], bio-layer interferometry [24], SPR [14–16], and quartz crystal microbalance with dissipation (QCM-D) [13, 25–27]. Many of these methods report low micromolar to nanomolar dissociation constants ( $K_D$ s) for the binding affinity between FG Nups and TFs [13–16, 20]. Although FG Nups are grafted onto a tubular surface in the actual NPC, and so such surface grafted systems seem consistent with the situation *in vivo*, the strong affinities observed in these experiments are at odds with the fast transport rates (~5–20 ms translocation time) seen *in vivo* [28–34]. Recently, we and others have reported in-solution affinities between TFs and individual FG motifs, whose per-FG-motif  $K_D$ s were in the millimolar range, compatible with the rapid kinetics of TF translocation through the NPC [17–19]. We also found that multiple low-affinity interactions can yield a higher overall interaction specificity than monovalent ones without compromising a high on-off rate of individual FG motifs [19]. Thus, one motivation of this work was to investigate the cause of these discrepancies in affinity measurements conducted by various methods.

As outlined by Schuck and Zhao, analysis of multivalent interactions by surface-based methods require extra care because of potential complexities of the binding mechanism on the surface; in some cases rendering the results “impossible to realistically interpret” [35]. In addition, (i) it is often difficult to quantify the amount or the density of protein conjugated to the surface; (ii) conjugated surfaces usually have an inhomogeneous distributions of ligands [35]; (iii) the degree and the effect of analyte retention on the surface after a binding experiment is often not assessed; (iv) mass transport limitations can significantly affect measurements of binding kinetics when using SPR and QCM-D, and are often overlooked [35–37]; (v) change in protein conformation or denaturation upon binding to surfaces can occur [38, 39], and (vi) macroscopic effects of surface crowding, especially in the context of multivalency, are not trivial to adequately address and quantify for surface-based methods [35].

A well-characterized model FG-TF system, Nsp1FG (the FG repeat region of Nsp1, an FG Nup containing at least 35 FG repeats) and Kap95 (a TF), was used to investigate some of the complexities outlined above. Nsp1 is the most abundant FG Nup in budding yeast (*S. cerevisiae*) and consists of two distinct FG regions: an N-terminal FG-type repeat region rich in polar amino acids such as asparagine, and the central FxFG-type repeat region that is rich in charged amino acids and has a highly conserved repeat sequence [40]. Kap95 belongs to a major class of TFs called karyopherins, and mediates the main canonical nuclear import pathway. Collectively, Kap95-Nsp1FG interactions mediate a large fraction of nucleocytoplasmic trafficking [41]. Karyopherins are comprised almost entirely of superhelical alpha-solenoids. Co-crystal structures with FG repeat peptides indicate that their interaction is mediated through the insertion of the phenylalanine from an individual FG motif into a cleft formed between adjacent alpha-helices on the outer surface of the solenoid [10, 42–44]. Kap95 is

thought to have multiple binding sites for FG motifs, though the exact number of binding sites is unknown (its paralog, Crm1, is reported to have eight FG-interaction sites [45]). Interactions between Nsp1 and Kap95 have been extensively characterized by various methods, including crystallography and NMR [10, 12, 15–17, 20, 42–44, 46, 47]. In this study, the Nsp1FG-Kap95 interaction was analyzed by three commonly used surface-based methods: AFM, QCM-D and SPR. AFM has been employed to characterize the nanomechanical properties of proteins, including FG Nups [21–23]. QCM-D and SPR can monitor binding of analytes to ligands anchored to the surface of their sensors in real time and have also been used to study FG Nups [13–16, 25–27]. The results obtained in this study qualitatively replicated earlier results using the same methods [13–16, 21–23, 25–27]; however, our results implicate macroscopic and likely non-biological physical events, notably mass transport limitations, which must therefore be accounted for in any analysis utilizing similar methods.

## Materials and methods

### Materials

HS-(CH<sub>2</sub>)<sub>11</sub>-EG<sub>3</sub>-OH (hPEG) and HS-(CH<sub>2</sub>)<sub>11</sub>-EG<sub>3</sub>-OCH<sub>3</sub> (mPEG) were purchased from Prochimia (Sopot, Poland). (3-aminopropyl)-trimethoxysilane was purchased from Gelest, Inc. (Morrisville, PA). Solution P: 18 mg/ml phenylmethylsulfonyl fluoride (PMSF), 0.3 mg/ml pepstatin A in ethanol, cOmplete EDTA-free protease inhibitor cocktail (PIC) (Roche Applied Science). All other chemicals were purchased from Sigma-Aldrich Co. (Saint Louis, MO), as ethylenediaminetetraacetic acid (EDTA), sodium dodecyl sulfate (SDS), 2-mercaptoethanol (βME), tris-(2-carboxyethyl)phosphine (TCEP). The buffer solutions prepared for the experimental work were: (i) PB: 0.01 M phosphate buffer, pH 7.4; (ii) PB-E: PB and 0.01 M EDTA; (iii) PBS: PB and 2.7 mM KCl and 137 mM NaCl<sub>2</sub>, pH 7.4; (iv) PBS-ET: PBS, 10 mM EDTA and 5 mM TCEP; (v) TB: 20 mM HEPES, 110 mM KOAc, 2 mM MgCl<sub>2</sub>, 10 μM CaCl<sub>2</sub> and 10 μM ZnCl<sub>2</sub>, pH 7.4; (vi) TBT: TB and 0.1% v/v Tween 20; (vii) TBT-D: TBT and 5 mM DTT; (viii) TBT-PVP: TBT and 0.3% (w/v) polyvinylpyrrolidone; (ix) HUT: 50 mM HEPES, 8 M urea and 0.5% Tween 20. All buffers were prepared fresh and filtered through a 0.22 μm polyethersulfone membrane Express Plus from Millipore (Billerica, MA). Compressed N<sub>2</sub>, He and O<sub>2</sub> were supplied by Airgas (Albany, NY).

### Protein purification

The expression and purification of Nsp1FG construct containing C-terminal cysteine residue followed by hexa-histidine tag was conducted as previously described [19, 20]. Cells expressing FG constructs (S1 Text) were thawed and resuspended in 30 ml of lysis buffer (20 mM HEPES-KOH pH 7.4, 150 mM NaCl, 1% solution P, 1x PIC) including 8 M urea. Cells were lysed by Microfluidizer (Microfluidics) and the lysate was clarified by centrifugation for 1 h at 192,838 g in a Type 50.2 Ti rotor (Beckman) at 4°C. The supernatant was filtered through a 0.22 μm or 0.45 μm filter depending on its viscosity and was loaded into a 10 ml TALON Sepharose resin (GE Healthcare) column. The resin was washed with 50 ml of (i) lysis buffer containing 8 M urea, (ii) lysis buffer containing 3 M urea, and with (iii) lysis buffer containing 10 mM imidazole and 3 M urea. The protein was eluted in lysis buffer containing 250 mM imidazole and 3 M urea. Eluted fractions were analyzed by SDS-PAGE. Fractions containing the protein were pooled and concentrated by centrifugal concentrators with 3 kDa molecular weight cutoff (EMD Millipore). The sample was polished by gel filtration (120 ml Superdex200) in 20 mM HEPES-KOH pH 7.4, 150 mM NaCl, 1 mM EDTA, 50 μM TCEP, 10% glycerol. Fractions containing the protein were pooled, concentrated, and, dialyzed against 20 mM

HEPES-KOH pH 7.4, 300 mM NaCl, 1 mM EDTA, 50  $\mu$ M TCEP, 20% glycerol. The sample was frozen with liquid nitrogen and stored at  $-80^{\circ}\text{C}$ .

Cells expressing GST-Kap95 were thawed and resuspended in TBT-D. The cells were lysed, and the lysate was cleared in the same manner as FG constructs above. Cleared lysate was loaded onto a glutathione-sepharose (GE Healthcare) column (GST-column) equilibrated with TBT-D. The resin was washed with 100 ml of (i) TBT-D, (ii) TBT-D containing 500 mM NaCl, and (iii) TBT-D. GST-Kap95 was eluted with 90 ml of 100 mM Tris-HCl pH 8.5, 20 mM glutathione. Eluted fractions were analyzed by SDS-PAGE and fractions containing GST-Kap95 were pooled. The pooled sample was then dialyzed against Buffer A (20 mM HEPES-KOH pH 6.8, 150 mM KCl, 2 mM  $\text{MgCl}_2$ ). GST was cleaved off by biotinylated thrombin (EMD Millipore), and enzyme was removed by streptavidin sepharose resin (EMD Millipore) following the manufacturer's instructions. Cleaved GST was removed by the regenerated GST column, and the flow through containing Kap95 was collected. The sample was then concentrated by 30k MWCO Centricon (Millipore) and gel filtered in Buffer A containing 10% glycerol. Fractions containing Kap95 were pooled, concentrated by 50k MWCO Centricon (Millipore) and dialyzed against Buffer A supplemented with 5 mM DTT and 20% glycerol overnight. The sample was frozen with liquid nitrogen and stored at  $-80^{\circ}\text{C}$ .

### Atomic force microscopy (AFM)

All force measurements were performed using the MFP-3DTM atomic force microscope (Asylum Research, Santa Barbara, CA) and the collected data were analyzed using IGOR Pro 6 (WaveMetrics, Inc., Lake Oswego, OR). Gold-coated surfaces were prepared by coating glass coverslips (0.20 mm, Corning, NY) with 15 nm of titanium (Ti, 99.999% International Advanced Materials, Spring Valley, NY) followed by 50 nm of gold (99.999%, International Advanced Materials) using the electron beam evaporator under a pressure of less than  $10^{-6}$  Torr. Nsp1FG solutions were first centrifuged for 10 min at 90,000 rpm in a TLA 100 rotor (Beckman) at  $4^{\circ}\text{C}$ , to remove possible precipitates occurred during protein storage. Two different protocols were followed in order to form either a sparse or a dense layer of Nsp1FG on the surface, sNsp1FG or dNsp1FG, respectively. For sparse sNsp1FG samples, gold-coated surfaces were: (i) Passivated with 2 mM hPEG for 5 min at RT; (ii) rinsed with EtOH and dried with  $\text{N}_2$ ; and finally (iii) incubated with reduced Nsp1FG solution for 48 h at  $4^{\circ}\text{C}$ . The reduced Nsp1FG solution was prepared by diluting the centrifuged Nsp1 sample to a concentration of 10  $\mu\text{g}/\text{ml}$  in PBS and incubated with 1 mM TCEP for 1 h at  $4^{\circ}\text{C}$ . For dNsp1FG samples, we modified a previously published protocol [48]. Gold-coated surfaces were: (i) incubated with reduced Nsp1FG solution for 1 h at  $4^{\circ}\text{C}$ ; (ii) soaked in 8 M urea in TBT for 30 min at RT; and finally (iii) incubated with 2 mM hPEG, 5 mM TCEP and 8 M urea for 48 h at  $4^{\circ}\text{C}$ . The reduced Nsp1FG solution was prepared by buffer exchanging the centrifuged Nsp1FG sample into TBT using Microcon centrifugal filter units (Millipore Corporation, Bedford, MA), concentrated to  $\sim 0.4$  mg/ml and incubated with 5 mM TCEP for 1 h at  $4^{\circ}\text{C}$ .

For sNsp1FG, single molecule force spectroscopy (SMFS) scans [49–53] were obtained in the so-called “Force–Volume (FV) mode” [54, 55] using biolevers RC-150-VB (Olympus, Center Valley, PA). The cantilevers were calibrated before each experiment, using previously described 3-steps procedure [56]. Spring constants were within 10% error from the ones supplied by the manufacturer. A FV-data set consisted of an array of 1,600 ( $40 \times 40$ ) force measurements, scanning in contact mode at 1  $\mu\text{m}/\text{s}$  an area of  $5 \times 5 \mu\text{m}^2$ , with each pixel point spanning an approximate width of 125 nm in both X and Y. The trigger force was set to 500 pN.

For dNsp1FG, SMFS scans were obtained in FV mode using gold coated silicon nitride cantilevers carrying a borosilicate glass sphere, diameter = 10  $\mu\text{m}$ , and a nominal spring constant of 60 pN/nm (Novascan, Ames, IA). The cantilevers were calibrated before each experiment. A FV-data set consisted of an array of 900 (30 x 30) force measurements, scanning in contact mode at 1  $\mu\text{m/s}$  an area of 5 x 5  $\mu\text{m}^2$ , with each pixel point spanning an approximate width of 167 nm in both X and Y. The trigger force was set to 1 nN.

### Quartz crystal microbalance with dissipation (QCM-D)

Frequency and dissipation measurements were performed using an E4 Auto system and its standard flow module QFM 401 (Biolin Scientific/Q-Sense, Linthicum, MD). All data were analyzed using the Sauerbrey model [57] for rigid layer coupled to the QCM-D sensor, or the Voigt-Voinova model [58] when the layer was characterized by a viscoelastic behavior. The latter is a build-in tool in QTools software (Biolin Scientific/Q-Sense, Linthicum, MD), and the fitting parameters are (i) the thickness, (ii) the elastic shear modulus and (iii) the shear viscosity of the layer.

Polished silicon dioxide quartz crystals with fundamental frequencies of 5 MHz (Qsx 303, Biolin Scientific/Q-Sense, Linthicum, MD) were washed with acetone for 10 min, isopropanol for 10 min, rinsed with ethanol and dried with  $\text{N}_2$ . Organic contaminants were removed by plasma cleaning (Atomflo 400L2 Plasma System, SurfX Technologies, Culver City, CA) at 120 W (30 L/min He, 0.2 L/min  $\text{O}_2$ ) for 4 min. Plasma treatment also provided a high density of hydroxyl functionalities suitable for subsequent silane modification. Silanization was performed ex-situ by (i) immersing the sensors in 2% v/v (3-aminopropyl)-trimethoxysilane solution in acetone, for 10 min at RT, to introduce reactive amine moieties; (ii) washing with acetone; (iii) rinsing with deionized  $\text{H}_2\text{O}$ ; (iv) drying with  $\text{N}_2$ ; and (v) curing at 100°C for 30 min. The sensor was then placed in the QCM-D flow module chamber for (i) succinimidyl 4-(p-maleimidophenyl)-butyrate (SMPB) conjugation, a bifunctional crosslinker containing NHS ester and maleimide moieties, converting the amine-reactive surface into a maleimide-reactive surface; and (ii) Nsp1FG conjugation via a thiol-maleimide coupling. Both reactions were performed in-situ and monitored in real time at 23°C. SMPB conjugation was performed at 100  $\mu\text{l/min}$  by (i) equilibrating the chamber with PB-E for 20 min; (ii) flowing 2 mM sulfo-SMPB in PB-E for 15 min; and (iii) washing with PB-E for 15 min. Sulfo-SMPB formed a rigid (i.e. dissipation  $\sim 0$ ) layer coupled to the surface, hence, according to the Sauerbrey equation, the adsorbed mass is proportional to a normalized decrease in frequency,  $\Delta F/n$  [Hz]. From the several experiments, the coupling of sulfo-SMBP resulted in  $\Delta F/n \sim 11$  Hz, corresponding to a density of  $\sim 2.5$  molecules/ $\text{nm}^2$ . Nsp1FG coupling was performed at 50  $\mu\text{l/min}$  by (i) equilibrating the chamber with PBS-ET for 20 min; (ii) flowing (and recycling) 0.1–0.2 mg/ml Nsp1FG in PBS-ET for 60 min; and (iii) washing with PBS-ET for 15 min, HUT for 5 min and finally PBS-ET for 15 min. Two passivation steps were finally included to remove any unreacted maleimide group by (i) flowing 5 mM mPEG in PBS-ET for 30 min; (ii) washing with PBS-ET for 10 min; (iii) flowing 50 mM  $\beta\text{ME}$  in PBS-ET for 30 min; and (iv) washing with PBS-ET for 10 min, HUT for 5 min and finally PBS-ET for 15 min.

Binding/unbinding experiments using Kap95, GST or BSA were performed at 50  $\mu\text{l/min}$  by (i) equilibrating the chamber with TBT-DG for 15 min; (ii) flowing the protein solution in TBT-DG for 10 min (binding step); (iii) washing with TBT-DG for 30 min (unbinding step); and finally (iv) washing with HUT for 5 min and TBT-DG for 15 min (regeneration step). A second set of experiments was performed to measure the affinity between Nsp1FG and Kap95. In order to minimize the effects of mass transfer (e.g. dilution effect when introducing the protein solution in the QCM-D chamber equilibrated with buffer), the runs were performed at

300  $\mu\text{l}/\text{min}$ . The binding step was 1 min, while the unbinding step was 15 min. The analysis to assess the effect of flow rate on the estimation the kinetic parameters is described in [S2 Text](#) and [S1 Fig](#).

### Surface plasmon resonance (SPR)

All SPR experiments were conducted on an XPR36 system (BioRad) using GLC sensor chips. The sensor was cleaned with 0.5% SDS, 50 mM NaOH, and 100 mM HCl as instructed by the manufacturer. A GLC sensor was activated to create amine-reactive surface using 50 mM sNHS/EDC (sulfo-N-hydroxysulfosuccinimide/1-ethyl-3-(3-dimethylaminopropyl) carbodiimide hydrochloride) chemistry at the flow rate of 30  $\mu\text{l}/\text{min}$  for 5 min. 5 mM aminopropyl-maleimide in HEPES Main Buffer (20 mM HEPES-KOH, pH 7.4, 150 mM NaCl, 1 mM EDTA) was applied to the surface to expose maleimides on the surface. C-terminally cysteine-tagged FG constructs were first diluted in HEPES Main Buffer with 20% glycerol, and then they were further diluted in Protein Conjugation Buffer (20 mM PIPES, pH 6.8, 150 mM NaCl, 1 mM EDTA, 0.8 M urea) to produce final ligand (FG Nup) solutions whose concentrations ranged between 8.75 ~ 140  $\mu\text{g}/\text{ml}$ . This two steps dilution ensured that all the final solutions were at the same pH and contained the same percentages of glycerol. FG constructs were then conjugated to the surface by the reaction between the maleimide and the sulfhydryl group on the cysteine residues at 30  $\mu\text{l}/\text{min}$ . The reaction was monitored and was manually terminated once the surface conjugation reached a desired level. In the 'bare surface' condition, protein was omitted, and plain Protein Conjugation Buffer was run over the surface. The surface was then flushed with 100 mM beta-mercaptoethanol in Protein Conjugation Buffer at 30  $\mu\text{l}/\text{min}$  for 8 min to quench unreacted maleimides and to passivate the surface. The conjugation step was completed by equilibrating the surface with HEPES Main Buffer at 30  $\mu\text{l}/\text{min}$  for 5 min, after which the instrument was switched to the analyte binding mode (i.e. rotation of the flow channel lid). Prior to the analyte binding experiments, the surface was equilibrated with TBT-PVP at 30  $\mu\text{l}/\text{min}$  for 3 min, washed with HUT solution at 30  $\mu\text{l}/\text{min}$  for 3 min, and re-equilibrated with TBT-PVP at 30  $\mu\text{l}/\text{min}$  for 3 min. The absolute amount of ligand molecules conjugated to the surface was practically difficult to assess, however, relative amounts of molecules on the surface was reported in response units (RU) as designated by the manufacturer. According to the manufacturer's estimate, 1,000 RU approximately corresponds to 1  $\text{ng}/\text{mm}^2$ .

Analytes were diluted in two steps as with the case for FG proteins. They were first with TBT supplemented with 20% glycerol, and then with TBT-PVP to designated concentrations. The concentration of analytes used for the binding experiments are noted in the respective figures. Binding experiment was conducted at 100  $\mu\text{l}/\text{min}$ . The duration of association phase was varied for different experiments, ranging between 15 and 120 s. Dissociation was monitored for 10 min. The surface was regenerated after each round of a binding experiment with HUT solution at 30  $\mu\text{l}/\text{min}$  for 2 min. The surface was then re-equilibrated with TBT-PVP at 30  $\mu\text{l}/\text{min}$  for 3 min before the next round of binding experiment. All binding experiments were conducted at 25°C.

The binding curves were analyzed by XPR36 software. The details of the used models were described previously [59].

## Results

### Establishing robust surface conjugation

In order to study FG Nup behavior and its interaction with TFs and non-specific proteins, we established a robust protocol to immobilize FG Nups on a surface. QCM-D experiments for

FG Nups have been conducted previously, where His-tagged FG Nups were conjugated non-covalently to a supported lipid bilayer (SLB) [13, 25–27]. Here, we used alternative protocols for direct, covalent attachment of FG Nups to surfaces because: (i) His-capturing moieties can be mobile when attached to lipids in the SLB, (ii) surface conjugation via His-tag is known to drift (i.e. His-tagged ligands detach and re-attach or drift away due to low affinity non-covalent bonds) [60], and (iii) it is not clear how indirect attachment of FG molecules via SLB would affect the overall surface behavior. Therefore, in this study, a single cysteine residue was inserted at the C-terminal end of the Nsp1FG domain construct to allow direct, covalent conjugation via the thiol moiety (-SH) to both gold and to chemically activated silica surfaces, so that only the FG molecules covalently attached to a surface can be examined. Following the convention of the SPR literature, the material conjugated onto the surface is designated “ligand” and the material flowing over the surface “analyte”.

The procedure for Nsp1FG conjugation to an amino-activated silica sensor is outlined in Fig 1A and representative QCM-D data is shown in Fig 1B. For gold surfaces, direct conjugation via the C-terminal cysteine was used. Although the analyte binding pattern on gold was similar to that on silica (S2 Fig), we chose silica sensors for protein binding experiments because they exhibited reduced non-specific binding compared to gold sensors (see below).

Polyethylene glycol-thiol (PEG-SH) was applied as a passivator [61], followed by a beta-mercaptoethanol treatment to deactivate unreacted maleimide moieties and to minimize non-specific binding. To find an appropriate passivator for protein binding experiments, different PEGs (i.e. number of PEG repeats and chemical groups) were tested against various analytes. Based on the results, a minimum of six PEG repeats were needed to produce an inert surface, while the terminal group did not have a visible effect on the inertness (S3 Fig). Thus, mPEG<sub>6</sub>-C<sub>2</sub>-SH was chosen as the passivator for our experiments. In addition, wash steps to remove any non-covalently bound material from the surface were included (S4 Fig).

To understand the physical properties of a densely packed Nsp1FG layer on a surface, the changes in frequency ( $\Delta F$ ) and energy dissipation ( $\Delta D$ ) resulting from the Nsp1FG conjugation were subjected to viscoelastic modeling. The Nsp1FG layer was viscoelastic, as indicated by a  $\Delta D/\Delta F$  ratio larger than  $1 \cdot 10^{-8} \text{ Hz}^{-1}$  [62] and by the spreading of the different harmonics (S5 Fig), consistent with results reported by others [13, 25–27]. The Voigt-Voinova model [58] was used to evaluate changes in layer thickness, shear modulus, and shear viscosity with time (Fig 1C). Varying the layer density estimate from 1,100 to 1,300  $\text{kg/m}^3$  (i.e. the effective density of the protein layer has to lie between 1,000  $\text{kg/m}^3$ , the value for water, and 1,330  $\text{kg/m}^3$ , the value for proteins, considering a partial specific volume of proteins close to 0.75  $\text{ml/g}$  [63–65]) did not significantly affect the estimated parameters. At low Nsp1FG density, the shear viscosity of the layer was close to that of pure water ( $\sim 0.001 \text{ Pa}\cdot\text{s}$ ) and increased to  $0.00135 \pm 0.00003 \text{ Pa}\cdot\text{s}$  as the Nsp1FG binding progressed when the layer density was set at 1,200  $\text{kg/m}^3$ . The shear modulus equilibrated at  $0.012 \pm 0.002 \text{ MPa}$  and the layer thickness at  $12.2 \pm 0.5 \text{ nm}$ . Although the thickness of the FG layer estimated here was smaller than those previously reported [13, 25–27], this could arise from how the FG-surface was set up, particularly the indirect attachment to the surface via a single lipid bilayer and the non-covalent attachment of FG proteins in those studies. Based on the mass conjugated on the surface ( $\sim 1,500 \text{ ng/cm}^2$ , or  $25.6 \text{ pmol/cm}^2$ ), the Nsp1FG layer behaves more like a polymer brush of 30 kDa PEG (which has shear viscosity below  $0.0014 \text{ Pa}\cdot\text{s}$  and shear modulus below  $0.1 \text{ MPa}$ ) than an agarose hydrogel (which has shear viscosity above  $0.0028 \text{ Pa}\cdot\text{s}$  and shear modulus above  $0.2 \text{ MPa}$ ) [66]. Moreover, a conjugated mass of  $\sim 1,500 \text{ ng/cm}^2$ , or  $25.6 \text{ pmol/cm}^2$  for Nsp1FG, is equivalent to an individual FG chain occupying  $15.4 \text{ nm}^2$  on average on the surface. This means that a single Nsp1FG chain occupies an area of  $2.2 \text{ nm}$  in radius, which is much smaller than its Stokes radius of  $\sim 9 \text{ nm}$  [40]. This also suggests that the FG domains are grafted at high surface density

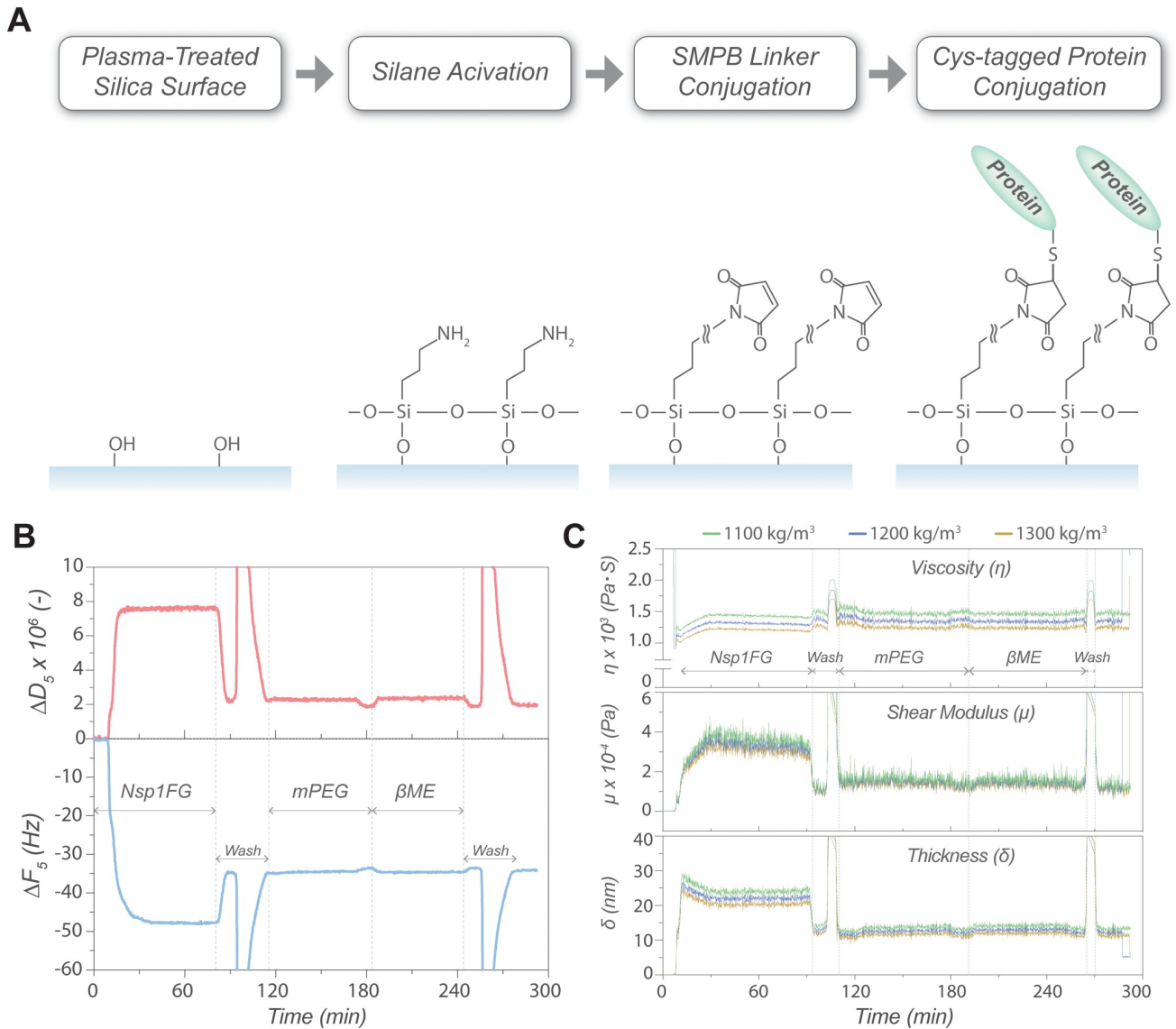


**Fig 1. Conjugation of Nsp1FG to a QCM-sensor.** (A) Chemical conjugation of Nsp1FG to a silica surface. (B) Representative sensorgram of Nsp1FG conjugation. Changes in resonance frequency ( $\Delta F_5$ ) (bottom, blue) and energy dissipation ( $\Delta D_5$ ) (top, red) for the 5<sup>th</sup> overtone recorded in real time. Nsp1FG conjugation step, wash, passivation with mPEG, and beta-mercaptoethanol treatment are indicated. (C) Viscoelastic modeling of the Nsp1FG surface at different density estimates (top: viscosity, middle: shear modulus, bottom: layer thickness).

<https://doi.org/10.1371/journal.pone.0217897.g001>

and form an extended molecular brush, because it is well understood that as the polymer grafting density on a surface increases, the closer packing of the polymers causes them to orthogonally elongate from the surface [67, 68]. Therefore, we were able to produce an FG-surface layer via direct, covalent attachment, whose properties are typical of a viscoelastic brush layer.

### Probing the FG Nup conjugated surface by AFM

To further assess the physical properties of Nsp1FG on a surface, AFM was employed in force mode to interrogate both single Nsp1FG chains (sNsp1FG) grafted at low density, as well as dense layers of Nsp1FG (dNsp1FG). Gold surfaces were chosen for the AFM work because (i) QCM-D experiments showed that the analyte binding properties of the gold surface was

similar to that of silica (S2 Fig); and (ii) the absence of a linker between the surface and the protein was preferred when stretching single protein molecules.

Substrate passivation, using hPEG<sub>6</sub>-C<sub>11</sub>-SH, was necessary (i) to minimize non-specific interaction between the gold-coated AFM cantilever tip and the gold surface and (ii) to vary Nsp1FG density on the surface for single molecule stretching. This step was optimized by testing different incubation times of hPEG<sub>6</sub>-C<sub>11</sub>-SH with the gold substrate (S6 Fig): a 5 min passivation step was included in the preparation of the samples discussed below.

All experiments were conducted either in PBS or TBT buffers and the schematic diagram for the AFM experiments is shown in Fig 2A. The Force-Volume (FV) map of sNsp1FG is shown in S7 Fig, where as many as 40 x 40 = 1,600 force curves per sample were collected. Up to a certain extension, ~50%, stretching of Nsp1FG occurred with forces less than 10 pN, indicating that Nsp1FG is an elastic molecule that can extend itself by ~50% without any significant force (Fig 2B, normalized data). Peaks showing reproducible stretching events were fitted using the worm-like chain (WLC) model [69, 70]:

$$F(x) = \frac{k_B T}{L_p} \left[ \frac{1}{4} \left( 1 - \frac{x}{L_c} \right)^{-2} - \frac{1}{4} + \frac{x}{L_c} \right] \quad (1)$$

where  $F(x)$  is the distance-dependent force [ $\text{kg} \cdot \text{m} \cdot \text{s}^{-2}$ ],  $x$  is the extension length [m],  $k_B$  is Boltzmann's constant [ $1.3806503 \cdot 10^{-23} \text{ m}^2 \cdot \text{kg} \cdot \text{s}^{-2} \cdot \text{K}^{-1}$ ],  $T$  is the temperature [K],  $L_p$  is the persistence length [m] and  $L_c$  is the contour length [m] of the chain (see Fig 2A). Examples of fitted data in PBS are shown in S8 Fig and the fitted values for  $L_p$  and  $L_c$ , as a function of adhesion force ( $F_{ad}$ ), are summarized in Fig 2C. The  $L_c$  represents the theoretical length of the stretched molecule. The wide variability of this parameter was due to the random interaction of the AFM cantilever tip with the covalently immobilized sNsp1FG, resulting in partial or full (i.e. ~250 nm, based on the AA sequence) stretching of the molecule. On the other hand,  $L_p$  is a measure of the rigidity of the polymer chain and it is an intrinsic property of the molecule (i.e. independent from  $L_c$  or  $F_{ad}$ ). The results showed a mean  $L_p$  of  $1.05 \pm 0.29$  nm in PBS and  $1.10 \pm 0.29$  nm in TBT buffer (S9 Fig), confirming the elastic behavior upon stretching of sNsp1FG, as previously shown for other FG Nups [21, 22]. Thus, the choice of buffer did not have a significant effect on the measurements. Similar results were obtained when stretching sNsp1FG at different pulling rates in PBS:  $1.05 \pm 0.29$  nm (1  $\mu\text{m/s}$ ),  $0.80 \pm 0.26$  nm (2  $\mu\text{m/s}$ ), and  $0.82 \pm 0.22$  nm (3  $\mu\text{m/s}$ ), confirming that  $L_p$  represents the intrinsic flexibility of Nsp1FG and is not caused by the mechanical stretching rate of the molecule (S10 Fig). When normalized to  $L_c$ , the retraction force curves collapsed into a “master curve”, confirming homogeneity of the Nsp1FG population and the elasticity of the individual Nsp1FG molecules (Fig 2B). Moreover the  $F_{ad}$  did not exceed 0.2 nN, well below the rupture force of a thiol-Au bond of ~1.4 nN [71], allowing stretching of Nsp1FG molecule without detachment. The persistence length measured here was larger than that measured for the human Nup153 FG region [21, 23], which probably reflects the sequence variation among different FG Nups.

AFM experiments were also performed on a dense brush layer of Nsp1FG, dNsp1FG, to simulate the high density of FG Nups in the NPC [11, 72–74]. The approach curves of the FV mapping scans were used to estimate the thickness of the dNsp1FG layer (Fig 2D). When the cantilever tip contacts a stiff surface, a sharp deflection of the approach curve is expected at the zero sample-tip distance. Since dNsp1FG formed a soft pliable layer on top of the stiff substrate, the cantilever tip sensed a repulsive force while indenting the dNsp1FG layer. This resulted in a curved deflection profile, before the sharp deflection when contacting the stiff sublayer. The onset of the repulsive force was used to estimate the dNsp1FG thickness of ~10 nm (Fig 2D, PEG-Nsp1). The thickness doubled when dNsp1FG was also on the cantilever

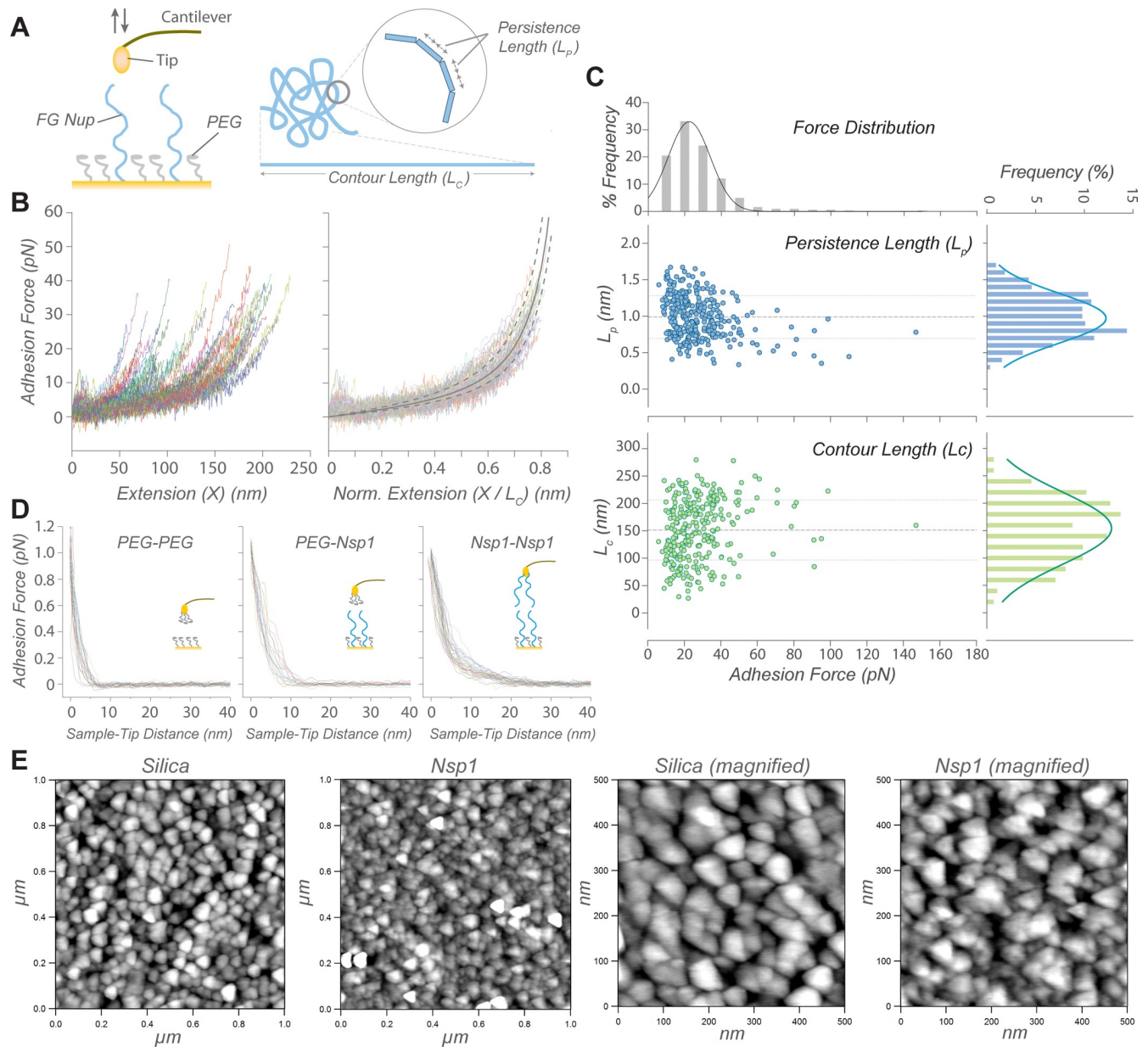


**Fig 2. Characterization of an Nsp1FG surface by AFM.** (A) Schematic diagram of Nsp1FG approach-pulling experiment and worm-like chain (WLC) model parameters. (B) Representative retraction curves during single Nsp1FG stretching (left), and superimposition of the normalized curves (right). Each curve represents a single stretching event. (C) WLC model estimates of persistence length ( $L_p$ ) and contour length ( $L_c$ ) scatter-plotted against the adhesion force. Their frequency distributions are plotted in respective histograms. (D) Approach curves for layer thickness measurements: Control (PEG-PEG, left), single Nsp1FG layer (PEG-Nsp1, middle), and double Nsp1FG layer (Nsp1-Nsp1, right).

<https://doi.org/10.1371/journal.pone.0217897.g002>

(Fig 2D, Nsp1-Nsp1) and was much higher than the hPEG<sub>6</sub>-C<sub>11</sub>-SH control of ~5 nm (Fig 2D, PEG-PEG). The AFM measurement may have underestimated the layer thickness if: (i) the AFM probe traveled through the top part of the FG Nup layer without a measurable deflection; (ii) the AFM probe sensed a positive deflection only after it compressed the layer; and (iii) the AFM did not reach a hard-contact with the substrate. Nevertheless, the Nsp1-Nsp1 measurement was roughly twice that of PEG-Nsp1 (Fig 2D) and AFM and QCM-D analyses provided

similar estimates of the FG layer thickness, suggesting internal consistency of our measurements of the FG-conjugated surface.

### Probing the FG-Kap95 interaction by QCM-D

To enable reproducible analysis from a FG surface, a regeneration procedure that yields maximum removal of remaining analyte at the end of each binding cycle was established. Two macromolecules were used for this optimization. The first, GST-Kap95, dimerizes via GST, providing increased valency for interaction, making it more likely to remain on the FG surface. The second, BSA, has been extensively employed as a test protein to check for surface inertness [75, 76]. Removal of both GST-Kap95 and BSA was achieved using 50 mM HEPES-KOH pH 7.4, 8 M urea, with 0.5% Tween (HUT buffer). While urea can denature the analyte, it is compatible with natively disordered FG constructs, and thus, is an appropriate addition to the regeneration buffer. Indeed, HUT completely regenerated the FG Nup surface (S4 Fig) and thus, was used at the end of every binding experiment.

Once conditions for reversible binding were established, the Nsp1FG surface was tested with different analytes to assess its specificity. Kap95 without the GST domain was able to reversibly bind the surface. Consistent with studies by others [13–16, 25–27], the Nsp1FG surface was essentially inert to non-specific proteins such as BSA and GST, and highly selective for Kap95 (Fig 3A). Thus, the expected qualitative characteristics of the FG-Kap95 interaction were recapitulated by QCM-D. However, further binding analyses revealed that a more detailed interpretation of the data is required.

### Influence of mass transport limitation

One of our major concerns was the effect of mass transport limitation, a well-known physical phenomenon among chemical engineers but less frequently examined in the biological literature [35, 36, 77]. Mass transport limitation is observed when the bulk flow over the sensor is insufficiently high relative to the binding kinetics of the protein-protein interaction under investigation to exclude influences of the transport process on the quantitation of kinetic parameters. Bulk flow transports analytes in the feed solution (i.e. mass transport) and the analytes diffuse from the bulk into the volume immediately adjacent to the surface, where they are close enough to interact with the ligands. When the rate of mass transport by bulk flow is sufficiently high, the buildup of analytes on the surface is fast, due to efficient diffusion from the bulk. The rate of protein absorption/binding actually depends on the concentration of the analyte in this region immediately adjacent to the surface, where the analytes are close enough to the surface layer for the interaction to happen, rather than the concentration in the bulk feed solution [35, 36, 77]; thus, when the bulk flow is too low, the concentration of the analyte in the region immediately adjacent to the surface is lower than that in the feed solution because the surface ligand ‘depletes’ the analyte locally, faster than the delivery by the bulk flow. Depletion by the ligand increases with higher ligand density as well as a higher on-rate of the protein-protein interaction. In the dissociation phase of a binding experiment, feed solution is usually a blank solution without any analyte. Under conditions where flow rates are slow and/or the ligand density is high, the escape rate of analytes from the surface can be slower than the ‘rebinding’ rate to the ligand, prolonging the apparent residence time of the analyte on the surface. Therefore, if mass transport limitation is significant but not taken into account, model fitting will yield erroneous kinetic parameter estimates.

There have been numerous studies utilizing surface-based systems to study protein-protein interactions involved in nuclear transport [13–16, 25–27], some of which indeed inferred the existence of mass transport limitations [13, 26, 27]. We initially became concerned about mass

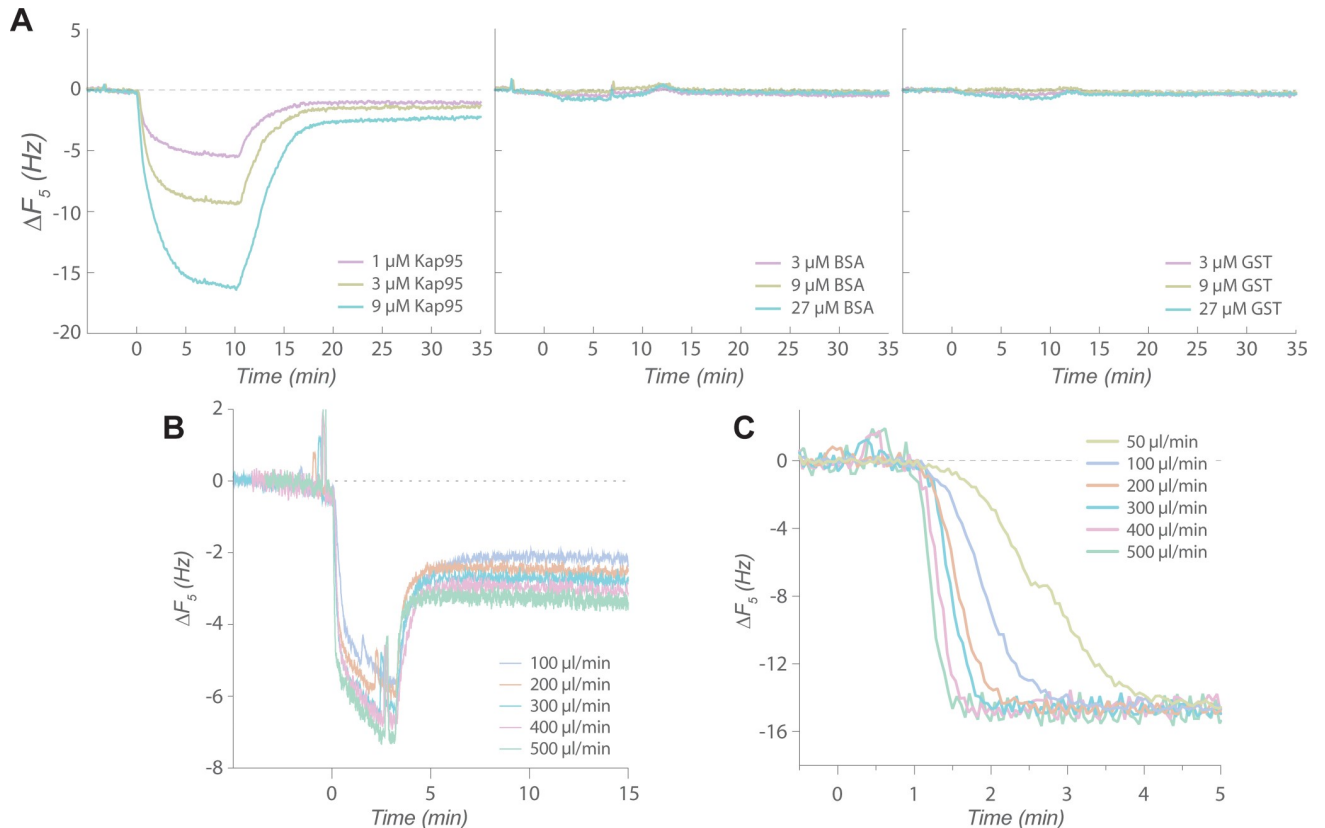


**Fig 3. Analyte binding assayed by QCM-D.** (A) Binding of different analytes on an Nsp1FG surface: Kap95 (left), BSA (middle), and GST (right). (B) Dependence of Kap95 binding to Nsp1FG surface on the flow rate. Changes in resonance frequency ( $\Delta F_5$ , 5th overtone) upon Kap95 binding are shown for different flow rates. (C) Sensing volume replacement by glycerol solution at different flow rates (see main text). Changes in resonance frequency ( $\Delta F_5$ , 5th overtone) after introducing feed solution containing glycerol (without any analyte) are shown for different flow rates.

<https://doi.org/10.1371/journal.pone.0217897.g003>

transport limitation when we observed that the fraction of GST-Kap95 that dissociates from the surface in our QCM-D system was dependent on the length of the association phase (S11 Fig), i.e. on the saturation level of the surface at the onset of the dissociation phase [35]. Hence, we studied in more detail the effect of flow rate on Kap95 binding alone, which indeed also proved flow-rate-dependent: larger amounts of binding were observed at higher flow rates, indicating mass transport per unit time was limiting at lower flow rates (Fig 3B), and suggesting that there was a lag in the mixing of analyte in the sensing volume.

We suspected that the large sensing volume ( $\sim 40 \mu$ l) of the QCM-D was a major factor for mass transport limitation. Based on the physical dimensions of the reaction chamber, the actual flow rate close to the surface (at 10 nm) is estimated to be  $1/10^5$ th of the bulk flow, which even at high flow rates remains in the laminar region according to the manufacturer specifications (e.g. average flow velocity of 1.03 mm/s with Reynold's number of 1.2 at the maximum flow of 500  $\mu$ l/min). To accurately interpret binding/unbinding kinetics, the sensing volume must be replaced with the feed solution essentially instantaneously. Instead, a mixing lag exists before the concentration of the analyte in the chamber reaches that of the feed solution. Therefore, we measured the extent of mixing lag at various flow rates by replacing an aqueous buffer with one containing glycerol. The glycerol-containing buffer results in a change in  $\Delta F$ , allowing us to monitor the liquid replacement in real time in the absence of analytes (Fig 3C). A concentration of glycerol of 3% was sufficient to induce a significant change in  $\Delta F$ ,

yet minimizes the effect of higher density and viscosity. It took ~30 s to replace the entire sensing volume even at 500  $\mu\text{l}/\text{min}$ , implying that only ~3% of the volume is replaced every second. Such a time scale is many orders of magnitude greater than that of most biochemical reactions, including the FG-TF interactions [17–19, 47]. Moreover, a simple, semi-quantitative analysis suggests that neglecting this mixing lag, i.e. the mass transport limitation issue, can underestimate the kinetic parameters by two orders of magnitude or higher when one assumes a simple Langmuir binding model (S2 Text).

### Mass transport limitation in SPR experiments

Analogous experiments were also conducted with SPR to test if its smaller sensing volume would allow measurement of the same FG-TF interaction without mass transport limitation. Although the same conjugation protocol used for QCM-D could not be implemented due to the conjugation chemistry available for the SPR system (XPR36, BioRad), the conditions for the binding experiments were optimized to minimize non-specific binding to a bare surface passivated with beta-mercaptoethanol (S12 Fig). A segment of Nsp1FG that contains six repeats of the FxFG-type region (FSFG<sub>6</sub>) was used for SPR. The binding of analytes to FSFG<sub>6</sub> was consistent with our QCM-D experiments with Nsp1FG and FSFG<sub>6</sub> (see below), and also with previously reported SPR results [14–16]. We observed Kap95 to bind FSFG<sub>6</sub> reversibly, whereas non-specific proteins did not exhibit any significant binding (Fig 4A), suggesting that the SPR measurements were consistent with the QCM-D setup.

To test for the existence of mass transport limitation, we first analyzed the SPR sensorgrams. In the absence of mass transport limitation, all the normalized dissociation curves from different analyte concentrations should converge to a single exponential decay. However, normalized Kap95 dissociation curves deviated from a single exponential decay (Fig 4B). Instead, the characteristic signatures of mass transport limitation [35] were present, as evidenced by: (1) the curvature of the normalized dissociation curves being dependent on Kap95 concentration, and steeper at higher Kap95 concentrations; (2) the relative amount of Kap95 retained on the surface after a fixed time period increasing with the density of the surface ligand; and (3) the relative amount of Kap95 retained on a surface with constant ligand density increasing with the amount of Kap95 bound to the surface (i.e. extent of surface saturation) at the onset of the dissociation phase. These observations indicate that mass transport limitation was also present in the SPR experiments. Our numerical simulations also suggest that mass transport limitations can be induced for even simpler interactions in this type of SPR chamber (S3 Text, S14 Fig, and S2 Table).

We next assessed whether the SPR data can be interpreted by commonly used kinetic models and by a simple Langmuir isotherm. Fittings of our results to these models are summarized in S15 Fig and S2 Table. A simple pseudo-first order kinetic model did not fit well to the experimental binding curves, as indicated by the large  $\chi^2$ . Inclusion of the mass transport limitation term also did not improve fitting to a one-to-one model. Fitting was better for more complex models, specifically for the two-state model, where conformational change of the ligand-analyte complex is assumed, and for the heterogeneous ligand model, where two types of independent ligands are assumed. In contrast, the heterogeneous analyte model, where two types of independent analytes were assumed, did not fit well. The goodness of fit for each model tested here can be assessed visually in S15 Fig (see also S2 Table). The data could be fitted equally well by the two-state model and the heterogeneous ligand model, suggesting that the interpretation of the data depends on an arbitrary choice of the model in the absence of independently obtained mechanical information. The trend in our fitting results is similar to that found in

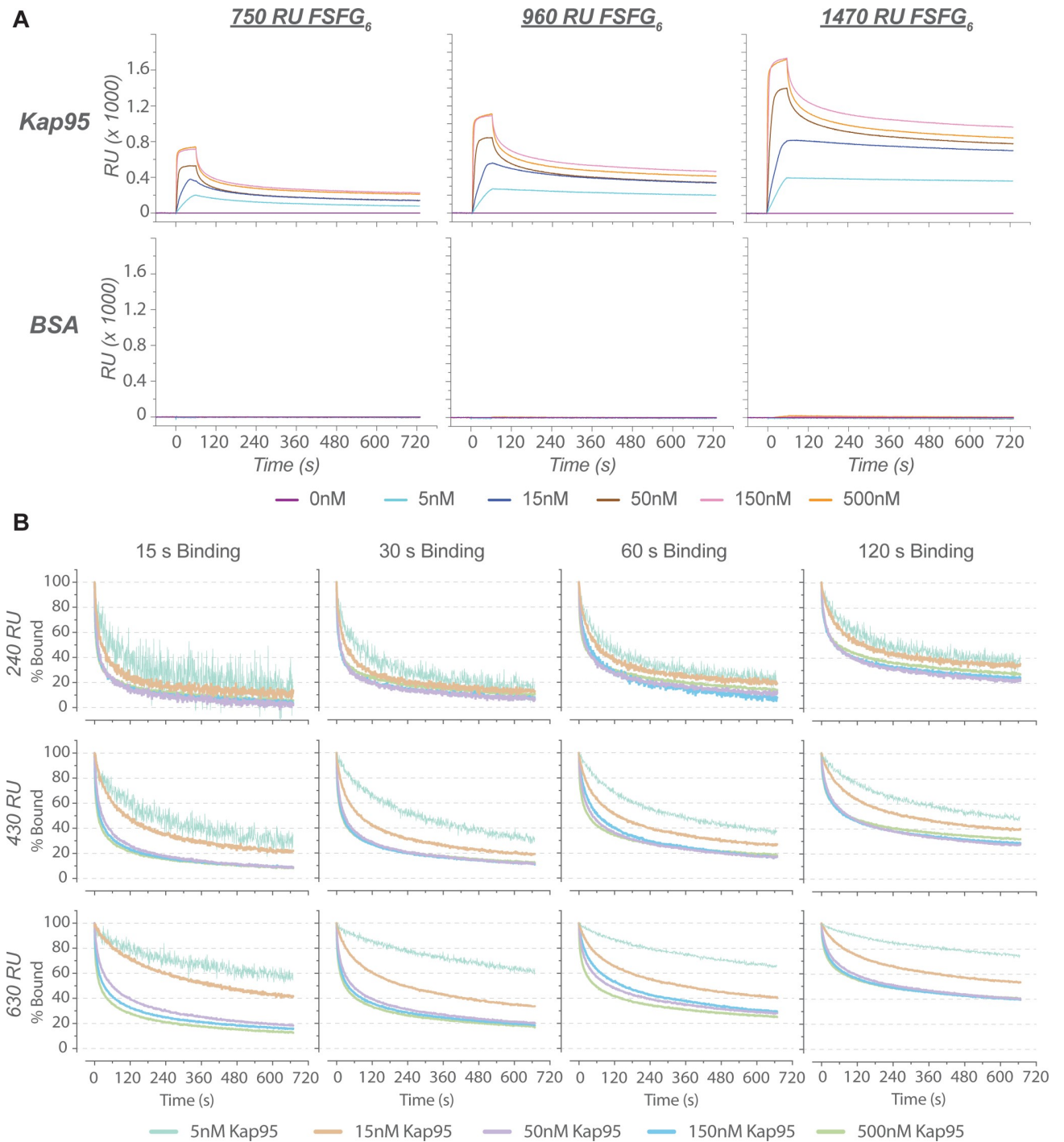


**Fig 4. Analyte binding assayed by SPR.** (A) Kap95 (top row) and BSA (bottom row) binding to a FSFG<sub>6</sub> surface at different surface ligand densities. RU (response unit. See [Materials and Methods](#)) values indicate the amount of FG protein on the surface: low (750 RU), medium (960 RU), and high (1470 RU), respectively. (B) Normalized dissociation curves of Kap95 to assess the existence of mass transport limitation. Different lengths of the association phase (columns) and different ligand densities (rows) are shown. Colors indicate different Kap95 concentrations. Respective unnormalized curves including the association phase are shown in [S13 Fig](#).

<https://doi.org/10.1371/journal.pone.0217897.g004>

previous works, where more complex models, including a Hill model [13, 25–27], yielded better fits to QCM-D binding curves than a simple Langmuir isotherm.

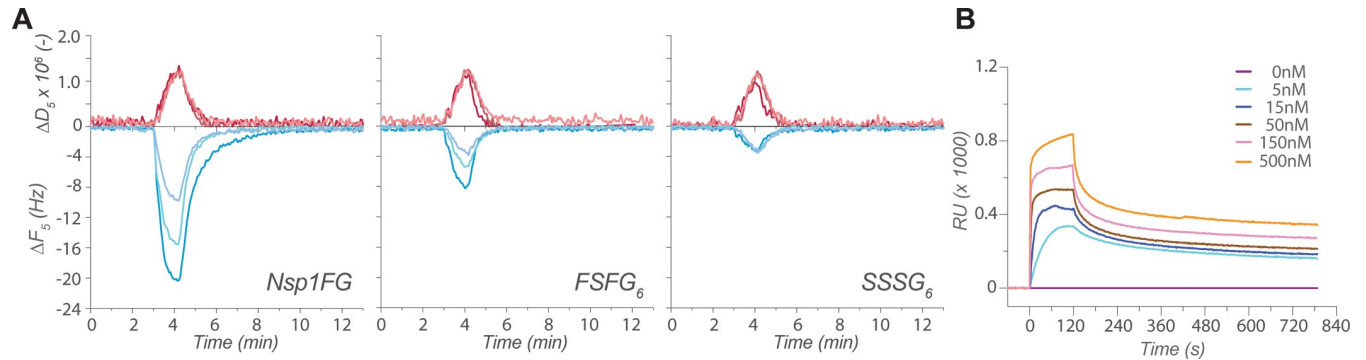


**Fig 5. Analyte binding experiments with SSSG<sub>6</sub> mutant variant.** (A) Kap95 binding on Nsp1FG (left), FSFG<sub>6</sub> (middle), and SSSG<sub>6</sub> (right) monitored by QCM-D. Changes in resonance frequency ( $\Delta F_5$ ) (bottom, blue) and energy dissipation ( $\Delta D_5$ ) (top, red) for the 5<sup>th</sup> overtone are shown. Kap95 concentrations are indicated by different shades of each color: light, medium, and dark shades indicate 1, 3, and 9  $\mu$ M Kap95, respectively. (B) Kap95 binding on SSSG<sub>6</sub> surface ( $\sim$ 920 response units (RUs) of SSSG<sub>6</sub> conjugated) by SPR. Kap95 concentrations are indicated by different colors.

<https://doi.org/10.1371/journal.pone.0217897.g005>

### Existence of more than one binding mode

In addition to the curve fitting analysis, further experiments were conducted to assess the biochemical relevance of our binding data by utilizing a mutant variant of FG constructs where the phenylalanines in FSFG constructs were replaced with serines (i.e. SSSG motifs). Structural studies indicate that FG Nups interact with karyopherins such as Kap95 by inserting the hydrophobic sidechain of their phenylalanine residues into the hydrophobic pockets of karyopherins, underscoring the requirement of the phenyl group in this interaction [43]. This Phe > Ser mutation was demonstrated to completely abolish interactions with TFs [19, 46, 78]. Thus, a six-repeats construct, SSSG<sub>6</sub>, was tested to determine if this total loss of interaction is observed in QCM-D and SPR experiments.

According to the QCM-D measurements, FSFG<sub>6</sub> and SSSG<sub>6</sub> layers behaved similarly, as they formed rigid layers due to their short length (S16 Fig), unlike the viscoelastic Nsp1FG layer (Fig 1C and S5 Fig). As expected, Kap95 bound strongly to FSFG<sub>6</sub>, though to a lesser extent than to Nsp1FG due to the reduced number of FG motifs (Fig 5A). More interestingly, Kap95 also interacted significantly with the surface-bound SSSG<sub>6</sub> construct, albeit to a lesser extent than the Phe counterpart, but greater in comparison to the binding pattern of non-specific analytes to Nsp1FG (Fig 4A). Similar observations were made in the SPR experiments: Kap95 bound to the SSSG<sub>6</sub> construct to a significant extent (Fig 5B), showing that Kap95 can be retained on the SSSG<sub>6</sub> surface despite the lack of FG motifs to mediate any specific binding. Since Kap95 did not bind to a bare SPR sensor under our experimental conditions (S12 Fig), we conclude that the Kap95 interactions are a result of unexpected non-specific binding to the SSSG<sub>6</sub>-conjugated surface, further complicating the measurements in conjunction with the influence of mass transport limitation.

### Discussion

FG Nup constructs and their interactions with Kap95 were systematically characterized by AFM, QCM-D, and SPR. Nsp1FG grafting conditions were optimized and cross-validated by AFM and QCM-D, which yielded a consistent picture on the viscoelastic behavior of Nsp1FG. Both QCM-D and SPR demonstrated the *apparent* specificity of the FG-grafted surfaces to the TF, Kap95. Therefore, robust experimental systems were set up to reproducibly collect data on TF binding to FG-grafted surfaces. The results from AFM, QCM-D, and SPR were in agreement with each other and with previous observations in the literature. However, our further

investigations demonstrated the existence of significant mass transport limitation and extra binding mode(s). The existence of mass transport limitations has been acknowledged in the nuclear transport field [13, 26, 27]. Indeed, the present work demonstrates the importance of taking mass transport limitations properly into account, but also the importance of considering unexplained physical phenomena that are implicit in the binding data. One could attempt to infer microscopic mechanisms that produced the binding curves, however, such deconvolution processes require assumptions about those mechanisms (e.g. what processes exist and how they depend on each other, along with all their parameters). While there have been attempts to model the generative process of the surface binding data, we and others found that the underlying dynamics of the “fuzzy” FG-TF interactions to be quite complex [17–19]. Since it is difficult to validate the assumptions we would have to make to model the surface binding data, we opted out from making such inferences in this work.

### Complexities of FG-TF binding reactions on a surface

Mass transport limitation is a significant but often overlooked issue in the field of SPR and QCM-D [35]. Although we observed that our surface-bound FG layers were selective for Kap95, the binding reaction appeared to be affected by mass transport limitation with both QCM-D and SPR. The likely contributing causes to this mass transport limitation include: (i) the physical scale of the flow systems, introducing a mixing lag, (ii) fast kinetics of FG-TF interactions, and (iii) the high multivalency of TFs and FG Nups that facilitates rebinding. The charge properties of the interactors may also affect their bulk mass transport behavior. The dimension of the QCM-D sensor is relatively large (millimeter ~ centimeter range), so that it takes ~30 s to replace the entire sensing volume of the chamber (Fig 3C), which resulted in the flow-rate-dependent binding of Kap95 (Fig 3B). In an attempt to alleviate the effect of mass transport limitation, we used SPR to study FG-TF interaction; its sensing volume is four orders of magnitude smaller than that of QCM-D chamber. However, our SPR experiments still appeared to suffer from a significant mass transport limitation (Fig 4). In addition, the apparent interaction of SSSG<sub>6</sub> with Kap95 suggests the existence of an FG-independent binding mode, further complicating the analysis of the data (Fig 5).

Although our results do not necessarily invalidate SPR and QCM-D for studying the physical properties of such surface layers, they indicate that data garnered using these methods must be interpreted with extreme care when studying a complex interaction, such as the one here with rapidly interacting proteins, when the surface density of ligand binding sites are high, thick and viscous. This is especially relevant in studying IDPs. Indeed, FG-TF interaction dynamics at the molecular level were shown to be even faster than the ~milliseconds time scale of NMR experiments [19], with association rate constant estimated to be  $\sim 1.5 \cdot 10^9 \text{ M}^{-1} \cdot \text{s}^{-1}$  [18]. Thus, the length scale and time-scale of SPR and QCM-D are too large to resolve any of the underlying molecular events considered here. Furthermore, the models tested with data from SPR largely underestimates the fastest component; the fastest rate estimated from the kinetic model fits was  $\sim 3.0 \cdot 10^6 \text{ M}^{-1} \cdot \text{s}^{-1}$  (S2 Table), a rate similar to  $k_{on}$  of the fast phase of the “two-phase” model reported in previous studies [15, 16], but which is orders of magnitude slower than the molecular rate mentioned above. We considered equilibrium analysis because of its time-independence. However, it proved difficult to establish if binding even reached an equilibrium with QCM-D, as the deposition of analytes continued to bind on a time-scale of minutes (S11 Fig). Moreover, our data suggests the existence of multiple types of binding events, and thus, any estimation of dissociation constant(s) would be heavily model-dependent, underscoring the limitation of extracting mechanistic information of a complex binding reaction solely from SPR and QCM-D sensorgrams. Thus, we did not attempt to draw any

quantitative conclusions from these data regarding the mechanism of nuclear transport. In addition, previously reported high affinities for FG-TF interactions from surface-based methods [8–16, 20] require re-evaluation in this light. The reported  $K_D$ s in those studies reflect the ‘residence time’ of TFs in FG layers (see below) rather than purely the binding mechanism at the molecular level. In a related topic, we recently emphasized the distinction between the global residence time of a protein in a loose protein-protein interaction (i.e. how long the two molecules stay associated with each other) and the half-life of an individual per-site interaction (i.e. how long an *individual bond* involved in the interaction persists) [17–19].

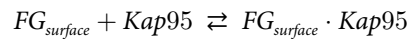
Understanding the multivalency of the FG-TF interactions on a surface is also difficult. In our recent study, we deconstructed the multivalency of interactions between FxFG-type constructs and another transporter, NTF2, in solution by NMR and ITC [19]. The majority of the FG-TF complexes characterized were binary ones (i.e. one FG repeat containing molecule and one TF molecule are involved), which behaved independently of each other on average, so the entropic effect of multivalency at the molecular level could be characterized well by ITC [19]. In contrast, understanding the effect of multivalency is not trivial to deconstruct on the densely-grafted FG surface we characterized here. Because any constraint on an intrinsically disordered FG chain is inherently entropically unfavorable [19], transient crosslinking of multiple FG chains via a TF would potentially have a larger entropic consequence on a surface than in solution. What would compensate for this at binding equilibrium on a surface is not clear and difficult to assess.

### Phenomenological $K_D$ s and microscopic mechanisms

Following the discussion above, we argue that it is not possible to accurately obtain microscopic  $K_D$  (s) for a complex binding reaction(s) simply based on a sensorgram without knowing the exact mechanism of binding on the surface-bound layer. The use of simple Langmuir isotherms to describe such complex reactions only yields ‘phenomenological (or apparent)  $K_D$ s’, which may be useful for estimating the partitioning of analytes between bulk flow and surface layer but do not provide precise thermodynamic information about the binding mechanism. Indeed, in the nuclear transport field, Richter and others have noted that their FG-TF binding data from QCM-D are “consistent with the presence of a spectrum of binding sites that cover a range of affinities,” suggesting the phenomenological nature of  $K_D$ s derived from such analytical models [13, 27]. For a complex protein-protein interaction, it is generally very difficult to accurately determine (i) the number of different binding mechanisms, (ii) the dependencies of such mechanisms on each other, (iii) the relative contributions to the overall binding curve from each mechanism, and (iv) their individual kinetic and thermodynamic parameters. A simple Langmuir isotherm, or even the simplest form of the Hill equations that is commonly used, would not properly represent such complex interactions [79]. Our experiments indicate that there are at least three kinds of physical events that contribute to the sensorgrams: FG-dependent binding, FG-independent binding, and mass transport limitation. In a case like this, where mass transport limitation is further complicated by multivalency, it is also difficult to estimate the extent of rebinding events within the surface layer because it is not manifest in the sensorgram. For instance, it is not possible to distinguish species with a long half-life of complexation from those that are simply retained on the surface by way of frequent rebinding. If the model does not properly account for the intricacies of multivalency in the presence of mass transport limitation, it would appear as if the binding is of high affinity with slow dissociation rates, leading to a misinterpretation of the data. Thus, phenomenological  $K_D$ s can be useful in describing macroscopic behaviors, but inferring their underlying mechanisms and their corresponding kinetic and thermodynamic parameters requires a set of

assumptions; hence, soundness of such models fundamentally depends on the validity of the assumptions they make, regardless of their mathematical sophistication [80].

Avidity, which is often loosely defined as the cumulative gain in affinity due to increased valency of participants in an interaction, is another metric relevant in multivalent systems. It is calculated as the ratio of the  $K_D$  of a monovalent system to that of a multivalent system of the same underlying ligand-receptor pair [81]. By grafting FG constructs with different numbers of FG motifs, one could measure and calculate avidity using apparent  $K_D$ s for the following surface-level binding reactions, e.g.:



The subscript in the reaction equation signifies that it is the FG surface that is considered as the reactant here. This particular avidity would be useful if one wishes to compare macroscopic behavior of the surface as a function of underlying multivalency, however, it is not informative in understanding the molecular details of the FG-Kap95 interaction. Furthermore, it is not trivial to deconstruct the multivalency of FG-TF interactions as we recently demonstrated using in-solution methods [19].

The above considerations are particularly relevant for analyzing IDPs, such as FG Nups. IDPs are known to have a broad spectrum of behaviors compared to folded proteins. The conformational space they can explore is immense and the mechanisms of interactions with their binding partners are diverse and complex, many of which are very difficult to track. For example, some IDPs bind to their partners by induced folding, while others maintain their intrinsic disorder in “fuzzy” interactions, like FG Nups [47, 82]. The mechanisms of these interactions are quite complex and the interaction mixture consists of ensembles of different configurational states, as suggested in our recent study [19]. Therefore, lacking the capability to finely resolve the mechanistic aspects of protein-protein interactions (e.g. distinct energy levels, defined interaction surfaces), the use of discrete analytical models on SPR and QCM-D data is probably not suitable for studying the mechanisms of IDP interactions. Exceptions are cases where QCM-D and AFM are used to study the morphological and viscoelastic features of a bulk IDP layer.

### Macroscopic instruments versus nanoscopic biological systems

The major cause of mass transport limitation in this study appeared to be the length- and time-scale of the experimental setup. The dimensions of QCM-D and SPR sensing volumes are orders of magnitude larger than the biological machineries they are exploring, with typical scales of tens of nanometers. For example, the FG-Nup filled central tube of the NPC spans ~50 nm, and thus is at least four orders of magnitude smaller than the above instruments. Under such nanoscopic environments, mass transport limitation would still exist, but its effect would scale similarly to those of molecular interactions and diffusion. However, under macroscopic systems such as SPR and QCM-D, mass transport limitation magnifies with the physical dimensions of the system (e.g. total number of binding sites increases with scale). The number of analyte binding/unbinding cycles it takes to randomly escape from the FG milieu is small at the nanometer scale. In contrast, the FG surface layers on SPR and QCM span microns to millimeters, so the number of on-off cycles to escape can be quite large (with a commensurate substantially longer residence time). Thus, the macroscopic dimensions of the instruments could well overshadow the molecular interactions and diffusion effects that are biologically relevant at nanoscopic scales. Solution studies *in vitro*, such as ITC, stopped-flow kinetics, NMR, and appropriately-scaled NPC mimics such as nanoscopic pores [48, 83–85] and DNA origami pores [86, 87] offer the possibility of studying FG-TF interactions at a scale more commensurate with that of nuclear transport *in vivo*.

## Supporting information

**S1 Text. Primary sequences of the protein constructs.**

(PDF)

**S2 Text. Estimating the impact of the mixing lag on the kinetic parameters in QCM-D experiments.**

(PDF)

**S3 Text. SPR—Simulating simple protein-protein interactions by multiphysics finite element model.**

(PDF)

**S1 Fig. Estimating the impact of the mixing lag on the kinetic parameters in QCM-D experiments.**

(PDF)

**S2 Fig. QCM-D—Comparison of gold and silica sensor.**

(PDF)

**S3 Fig. QCM-D—Comparison of PEG passivators.**

(PDF)

**S4 Fig. QCM-D—Surface regeneration.**

(PDF)

**S5 Fig. QCM-D—Different harmonics during Nsp1FG conjugation.**

(PDF)

**S6 Fig. AFM (volume force mapping)—Surface passivation with hPEG<sub>6</sub>-C11-SH.**

(PDF)

**S7 Fig. AFM—Force-map of Nsp1FG for single molecule stretching.**

(PDF)

**S8 Fig. AFM—Data fitting using the Worm Like Chain model.**

(PDF)

**S9 Fig. AFM—Nsp1FG pulling experiment in TBT buffer.**

(PDF)

**S10 Fig. AFM—Stretching Nsp1 in PBS at different pulling rates.**

(PDF)

**S11 Fig. QCM-D—GST-Kap95 binding with varying binding time.**

(PDF)

**S12 Fig. SPR—Non-specific binding on a bare surface passivated with beta-mercaptoethanol.**

(PDF)

**S13 Fig. SPR—Kap95 binding experiments.**

(PDF)

**S14 Fig. SPR—Numerical simulation of SPR binding curves.**

(PDF)

**S15 Fig. SPR—Fitting various kinetic models to binding curves.**

(PDF)

**S16 Fig. QCM-D—Conjugation of FSFG<sub>6</sub> and SSSG<sub>6</sub> to silica sensors.**

(PDF)

**S1 Table. SPR—Numerical simulation parameters.**

(PDF)

**S2 Table. SPR—Fitting kinetic and equilibrium models to binding curves.**

(PDF)

## Acknowledgments

We thank the High Throughput and Spectroscopy Resource Center at the Rockefeller University. We thank Drs. Roderick YH Lim, Larisa E. Kapinos, Ralph P Richter, Bart W Hoogenboom, David Cowburn, and Samuel Sparks for their helpful comments on the manuscript.

This work was supported by National Institutes of Health grants P41GM109824, R01GM112108 and R01GM117212.

## Author Contributions

**Conceptualization:** Ryo Hayama, Mirco Sorci, Georges Belfort, Brian T. Chait, Michael P. Rout.

**Data curation:** Ryo Hayama, Mirco Sorci, Joel L. Plawsky.

**Formal analysis:** Ryo Hayama, Mirco Sorci, John J. Keating IV, Joel L. Plawsky, Georges Belfort, Brian T. Chait.

**Funding acquisition:** Brian T. Chait, Michael P. Rout.

**Investigation:** Ryo Hayama, Mirco Sorci, Georges Belfort, Brian T. Chait, Michael P. Rout.

**Methodology:** Ryo Hayama, Mirco Sorci, John J. Keating IV, Lee M. Hecht, Joel L. Plawsky.

**Project administration:** Georges Belfort, Brian T. Chait, Michael P. Rout.

**Resources:** Ryo Hayama, Mirco Sorci, Lee M. Hecht, Georges Belfort, Brian T. Chait, Michael P. Rout.

**Software:** Ryo Hayama, Mirco Sorci, John J. Keating IV, Joel L. Plawsky, Georges Belfort.

**Supervision:** Joel L. Plawsky, Georges Belfort, Brian T. Chait, Michael P. Rout.

**Validation:** Ryo Hayama, Mirco Sorci, John J. Keating IV, Joel L. Plawsky.

**Visualization:** Ryo Hayama, Mirco Sorci, John J. Keating IV, Joel L. Plawsky.

**Writing – original draft:** Ryo Hayama, Mirco Sorci, Georges Belfort, Brian T. Chait, Michael P. Rout.

**Writing – review & editing:** Ryo Hayama, Mirco Sorci, Georges Belfort, Brian T. Chait, Michael P. Rout.

## References

1. Oldfield CJ, Dunker AK. Intrinsically disordered proteins and intrinsically disordered protein regions. *Annu Rev Biochem.* 2014; 83:553–84. Epub 2014/03/13. <https://doi.org/10.1146/annurev-biochem-072711-164947> PMID: 24606139.

2. van der Lee R, Buljan M, Lang B, Weatheritt RJ, Daughdrill GW, Dunker AK, et al. Classification of intrinsically disordered regions and proteins. *Chem Rev*. 2014; 114(13):6589–631. Epub 2014/04/30. <https://doi.org/10.1021/cr400525m> PMID: 24773235; PubMed Central PMCID: PMC4095912.
3. Beck M, Hurt E. The nuclear pore complex: understanding its function through structural insight. *Nat Rev Mol Cell Biol*. 2017; 18(2):73–89. Epub 2016/12/22. <https://doi.org/10.1038/nrm.2016.147> PMID: 27999437.
4. Aramburu IV, Lemke EA. Floppy but not sloppy: Interaction mechanism of FG-nucleoporins and nuclear transport receptors. *Semin Cell Dev Biol*. 2017; 68:34–41. Epub 2017/07/04. <https://doi.org/10.1016/j.semcdb.2017.06.026> PMID: 28669824.
5. Sakiyama Y, Panatala R, Lim RYH. Structural dynamics of the nuclear pore complex. *Semin Cell Dev Biol*. 2017; 68:27–33. Epub 2017/06/06. <https://doi.org/10.1016/j.semcdb.2017.05.021> PMID: 28579449.
6. Tetenbaum-Novatt J, Rout MP. The mechanism of nucleocytoplasmic transport through the nuclear pore complex. *Cold Spring Harb Symp Quant Biol*. 2010; 75:567–84. Epub 2011/03/31. <https://doi.org/10.1101/sqb.2010.75.033> PMID: 21447814.
7. Jovanovic-Talman T, Zilman A. Protein Transport by the Nuclear Pore Complex: Simple Biophysics of a Complex Biomachine. *Biophys J*. 2017; 113(1):6–14. Epub 2017/07/13. <https://doi.org/10.1016/j.bpj.2017.05.024> PMID: 28700925; PubMed Central PMCID: PMC5510711.
8. Delphin C, Guan T, Melchior F, Gerace L. RanGTP targets p97 to RanBP2, a filamentous protein localized at the cytoplasmic periphery of the nuclear pore complex. *Mol Biol Cell*. 1997; 8(12):2379–90. Epub 1997/12/17. PMID: 9398662; PubMed Central PMCID: PMC25714.
9. Ben-Efraim I, Gerace L. Gradient of increasing affinity of importin beta for nucleoporins along the pathway of nuclear import. *J Cell Biol*. 2001; 152(2):411–7. Epub 2001/03/27. <https://doi.org/10.1083/jcb.152.2.411> PMID: 11266456; PubMed Central PMCID: PMC2199621.
10. Bayliss R, Littlewood T, Strawn LA, Wentz SR, Stewart M. GLFG and FxFG nucleoporins bind to overlapping sites on importin-beta. *J Biol Chem*. 2002; 277(52):50597–606. Epub 2002/10/10. <https://doi.org/10.1074/jbc.M209037200> PMID: 12372823.
11. Gilchrist D, Mykytko B, Rexach M. Accelerating the rate of disassembly of karyopherin.cargo complexes. *J Biol Chem*. 2002; 277(20):18161–72. Epub 2002/02/28. <https://doi.org/10.1074/jbc.M112306200> PMID: 11867631.
12. Pyhtila B, Rexach M. A gradient of affinity for the karyopherin Kap95p along the yeast nuclear pore complex. *J Biol Chem*. 2003; 278(43):42699–709. Epub 2003/08/15. <https://doi.org/10.1074/jbc.M307135200> PMID: 12917401.
13. Eisele NB, Frey S, Piehler J, Gorlich D, Richter RP. Ultrathin nucleoporin phenylalanine-glycine repeat films and their interaction with nuclear transport receptors. *EMBO Rep*. 2010; 11(5):366–72. Epub 2010/04/10. <https://doi.org/10.1038/embor.2010.34> PMID: 20379223; PubMed Central PMCID: PMC2868541.
14. Schoch RL, Kapinos LE, Lim RY. Nuclear transport receptor binding avidity triggers a self-healing collapse transition in FG-nucleoporin molecular brushes. *Proc Natl Acad Sci U S A*. 2012; 109(42):16911–6. Epub 2012/10/09. <https://doi.org/10.1073/pnas.1208440109> PMID: 23043112; PubMed Central PMCID: PMC3479521.
15. Kapinos LE, Schoch RL, Wagner RS, Schleicher KD, Lim RY. Karyopherin-centric control of nuclear pores based on molecular occupancy and kinetic analysis of multivalent binding with FG nucleoporins. *Biophys J*. 2014; 106(8):1751–62. Epub 2014/04/18. <https://doi.org/10.1016/j.bpj.2014.02.021> PMID: 24739174; PubMed Central PMCID: PMC4008817.
16. Wagner RS, Kapinos LE, Marshall NJ, Stewart M, Lim RYH. Promiscuous binding of Karyopherinbeta1 modulates FG nucleoporin barrier function and expedites NTF2 transport kinetics. *Biophys J*. 2015; 108(4):918–27. Epub 2015/02/19. <https://doi.org/10.1016/j.bpj.2014.12.041> PMID: 25692596; PubMed Central PMCID: PMC4336380.
17. Hough LE, Dutta K, Sparks S, Temel DB, Kamal A, Tetenbaum-Novatt J, et al. The molecular mechanism of nuclear transport revealed by atomic-scale measurements. *Elife*. 2015; 4. Epub 2015/09/16. <https://doi.org/10.7554/eLife.10027> PMID: 26371551; PubMed Central PMCID: PMC4621360.
18. Milles S, Mercadante D, Aramburu IV, Jensen MR, Banterle N, Koehler C, et al. Plasticity of an ultrafast interaction between nucleoporins and nuclear transport receptors. *Cell*. 2015; 163(3):734–45. Epub 2015/10/13. <https://doi.org/10.1016/j.cell.2015.09.047> PMID: 26456112; PubMed Central PMCID: PMC4622936.
19. Hayama R, Sparks S, Hecht LM, Dutta K, Karp JM, Cabana CM, et al. Thermodynamic characterization of the multivalent interactions underlying rapid and selective translocation through the nuclear pore complex. *J Biol Chem*. 2018; 293(12):4555–63. Epub 2018/01/28. <https://doi.org/10.1074/jbc.AC117.001649> PMID: 29374059; PubMed Central PMCID: PMC5868264.

20. Tetenbaum-Novatt J, Hough LE, Mironska R, McKenney AS, Rout MP. Nucleocytoplasmic transport: a role for nonspecific competition in karyopherin-nucleoporin interactions. *Mol Cell Proteomics*. 2012; 11(5):31–46. Epub 2012/02/24. <https://doi.org/10.1074/mcp.M111.013656> PMID: 22357553; PubMed Central PMCID: PMC3418842.
21. Lim RY, Huang NP, Koser J, Deng J, Lau KH, Schwarz-Herion K, et al. Flexible phenylalanine-glycine nucleoporins as entropic barriers to nucleocytoplasmic transport. *Proc Natl Acad Sci U S A*. 2006; 103(25):9512–7. Epub 2006/06/14. <https://doi.org/10.1073/pnas.0603521103> PMID: 16769882; PubMed Central PMCID: PMC1480438.
22. Lim RY, Koser J, Huang NP, Schwarz-Herion K, Aebi U. Nanomechanical interactions of phenylalanine-glycine nucleoporins studied by single molecule force-volume spectroscopy. *J Struct Biol*. 2007; 159(2):277–89. Epub 2007/04/21. <https://doi.org/10.1016/j.jsb.2007.01.018> PMID: 17446086.
23. Lim RY, Fahrenkrog B, Koser J, Schwarz-Herion K, Deng J, Aebi U. Nanomechanical basis of selective gating by the nuclear pore complex. *Science*. 2007; 318(5850):640–3. Epub 2007/10/06. <https://doi.org/10.1126/science.1145980> PMID: 17916694.
24. Onischenko E, Tang JH, Andersen KR, Knockenhauer KE, Vallotton P, Derrer CP, et al. Natively Unfolded FG Repeats Stabilize the Structure of the Nuclear Pore Complex. *Cell*. 2017; 171(4):904–17 e19. Epub 2017/10/17. <https://doi.org/10.1016/j.cell.2017.09.033> PMID: 29033133; PubMed Central PMCID: PMC5992322.
25. Eisele NB, Andersson FI, Frey S, Richter RP. Viscoelasticity of thin biomolecular films: a case study on nucleoporin phenylalanine-glycine repeats grafted to a histidine-tag capturing QCM-D sensor. *Biomacromolecules*. 2012; 13(8):2322–32. Epub 2012/07/12. <https://doi.org/10.1021/bm300577s> PMID: 22780202.
26. Eisele NB, Labokha AA, Frey S, Gorlich D, Richter RP. Cohesiveness tunes assembly and morphology of FG nucleoporin domain meshworks—Implications for nuclear pore permeability. *Biophys J*. 2013; 105(8):1860–70. Epub 2013/10/22. <https://doi.org/10.1016/j.bpj.2013.09.006> PMID: 24138862; PubMed Central PMCID: PMC3797576.
27. Zahn R, Osmanovic D, Ehret S, Araya Callis C, Frey S, Stewart M, et al. A physical model describing the interaction of nuclear transport receptors with FG nucleoporin domain assemblies. *Elife*. 2016; 5. Epub 2016/04/09. <https://doi.org/10.7554/eLife.14119> PMID: 27058170; PubMed Central PMCID: PMC4874776.
28. Grunwald D, Singer RH. In vivo imaging of labelled endogenous beta-actin mRNA during nucleocytoplasmic transport. *Nature*. 2010; 467(7315):604–7. Epub 2010/09/17. <https://doi.org/10.1038/nature09438> PMID: 20844488; PubMed Central PMCID: PMC3005609.
29. Ribbeck K, Gorlich D. Kinetic analysis of translocation through nuclear pore complexes. *EMBO J*. 2001; 20(6):1320–30. Epub 2001/03/17. <https://doi.org/10.1093/emboj/20.6.1320> PMID: 11250898; PubMed Central PMCID: PMC145537.
30. Tu LC, Fu G, Zilman A, Musser SM. Large cargo transport by nuclear pores: implications for the spatial organization of FG-nucleoporins. *EMBO J*. 2013; 32(24):3220–30. Epub 2013/11/12. <https://doi.org/10.1038/emboj.2013.239> PMID: 24213245; PubMed Central PMCID: PMC3981140.
31. Yang W, Gelles J, Musser SM. Imaging of single-molecule translocation through nuclear pore complexes. *Proc Natl Acad Sci U S A*. 2004; 101(35):12887–92. Epub 2004/08/13. <https://doi.org/10.1073/pnas.0403675101> PMID: 15306682; PubMed Central PMCID: PMC156490.
32. Cardarelli F, Gratton E. In vivo imaging of single-molecule translocation through nuclear pore complexes by pair correlation functions. *PLoS One*. 2010; 5(5):e10475. Epub 2010/05/11. <https://doi.org/10.1371/journal.pone.0010475> PMID: 20454622; PubMed Central PMCID: PMC2862743.
33. Yang W, Musser SM. Nuclear import time and transport efficiency depend on importin beta concentration. *J Cell Biol*. 2006; 174(7):951–61. Epub 2006/09/20. <https://doi.org/10.1083/jcb.200605053> PMID: 16982803; PubMed Central PMCID: PMC162064387.
34. Kubitscheck U, Siebrasse JP. Kinetics of transport through the nuclear pore complex. *Semin Cell Dev Biol*. 2017; 68:18–26. Epub 2017/07/06. <https://doi.org/10.1016/j.semcdb.2017.06.016> PMID: 28676422.
35. Schuck P, Zhao H. The role of mass transport limitation and surface heterogeneity in the biophysical characterization of macromolecular binding processes by SPR biosensing. *Methods Mol Biol*. 2010; 627:15–54. Epub 2010/03/11. [https://doi.org/10.1007/978-1-60761-670-2\\_2](https://doi.org/10.1007/978-1-60761-670-2_2) PMID: 20217612; PubMed Central PMCID: PMC34134667.
36. Christensen LL. Theoretical analysis of protein concentration determination using biosensor technology under conditions of partial mass transport limitation. *Anal Biochem*. 1997; 249(2):153–64. Epub 1997/07/01. <https://doi.org/10.1006/abio.1997.2182> PMID: 9212867.
37. Wilczewski M, Van der Heyden A, Renaudet O, Dumy P, Coche-Guerente L, Labbe P. Promotion of sugar-lectin recognition through the multiple sugar presentation offered by regioselectively addressable

- functionalized templates (RAFT): a QCM-D and SPR study. *Org Biomol Chem*. 2008; 6(6):1114–22. Epub 2008/03/11. <https://doi.org/10.1039/b716214f> PMID: 18327340.
38. Anand G, Sharma S, Dutta AK, Kumar SK, Belfort G. Conformational transitions of adsorbed proteins on surfaces of varying polarity. *Langmuir*. 2010; 26(13):10803–11. Epub 2010/05/04. <https://doi.org/10.1021/la1006132> PMID: 20433160.
  39. Grimaldi J, Radhakrishna M, Kumar SK, Belfort G. Stability of Proteins on Hydrophilic Surfaces. *Langmuir*. 2015; 31(3):1005–10. <https://doi.org/10.1021/la503865b> WOS:000348689700016. PMID: 25533285
  40. Yamada J, Phillips JL, Patel S, Goldfien G, Calestagne-Morelli A, Huang H, et al. A bimodal distribution of two distinct categories of intrinsically disordered structures with separate functions in FG nucleoporins. *Mol Cell Proteomics*. 2010; 9(10):2205–24. Epub 2010/04/07. <https://doi.org/10.1074/mcp.M000035-MCP201> PMID: 20368288; PubMed Central PMCID: PMCPCMC2953916.
  41. Christie M, Chang CW, Rona G, Smith KM, Stewart AG, Takeda AA, et al. Structural Biology and Regulation of Protein Import into the Nucleus. *J Mol Biol*. 2016; 428(10 Pt A):2060–90. Epub 2015/11/03. <https://doi.org/10.1016/j.jmb.2015.10.023> PMID: 26523678.
  42. Bayliss R, Kent HM, Corbett AH, Stewart M. Crystallization and initial X-ray diffraction characterization of complexes of FxFG nucleoporin repeats with nuclear transport factors. *J Struct Biol*. 2000; 131(3):240–7. Epub 2000/10/29. <https://doi.org/10.1006/jsbi.2000.4297> PMID: 11052897.
  43. Bayliss R, Littlewood T, Stewart M. Structural basis for the interaction between FxFG nucleoporin repeats and importin-beta in nuclear trafficking. *Cell*. 2000; 102(1):99–108. Epub 2000/08/10. PMID: 10929717.
  44. Isgro TA, Schulten K. Binding dynamics of isolated nucleoporin repeat regions to importin-beta. *Structure*. 2005; 13(12):1869–79. Epub 2005/12/13. <https://doi.org/10.1016/j.str.2005.09.007> PMID: 16338415.
  45. Port SA, Monecke T, Dickmanns A, Spillner C, Hofele R, Urlaub H, et al. Structural and Functional Characterization of CRM1-Nup214 Interactions Reveals Multiple FG-Binding Sites Involved in Nuclear Export. *Cell Rep*. 2015; 13(4):690–702. Epub 2015/10/23. <https://doi.org/10.1016/j.celrep.2015.09.042> PMID: 26489467.
  46. Patel SS, Rexach MF. Discovering novel interactions at the nuclear pore complex using bead halo: a rapid method for detecting molecular interactions of high and low affinity at equilibrium. *Mol Cell Proteomics*. 2008; 7(1):121–31. Epub 2007/09/28. <https://doi.org/10.1074/mcp.M700407-MCP200> PMID: 17897934.
  47. Sparks S, Temel DB, Rout MP, Cowburn D. Deciphering the "Fuzzy" Interaction of FG Nucleoporins and Transport Factors Using Small-Angle Neutron Scattering. *Structure*. 2018; 26(3):477–84 e4. Epub 2018/02/13. <https://doi.org/10.1016/j.str.2018.01.010> PMID: 29429880; PubMed Central PMCID: PMCPCMC5929991.
  48. Jovanovic-Talisman T, Tetenbaum-Novatt J, McKenney AS, Zilman A, Peters R, Rout MP, et al. Artificial nanopores that mimic the transport selectivity of the nuclear pore complex. *Nature*. 2009; 457(7232):1023–7. Epub 2008/12/23. <https://doi.org/10.1038/nature07600> PMID: 19098896; PubMed Central PMCID: PMCPCMC2764719.
  49. Rief M, Gautel M, Oesterhelt F, Fernandez JM, Gaub HE. Reversible unfolding of individual titin immunoglobulin domains by AFM. *Science*. 1997; 276(5315):1109–12. Epub 1997/05/16. PMID: 9148804.
  50. Oesterhelt F, Oesterhelt D, Pfeiffer M, Engel A, Gaub HE, Muller DJ. Unfolding pathways of individual bacteriorhodopsins. *Science*. 2000; 288(5463):143–6. Epub 2001/02/07. PMID: 10753119.
  51. Rief M, Clausen-Schaumann H, Gaub HE. Sequence-dependent mechanics of single DNA molecules. *Nat Struct Biol*. 1999; 6(4):346–9. Epub 1999/04/14. <https://doi.org/10.1038/7582> PMID: 10201403.
  52. Rief M, Oesterhelt F, Heymann B, Gaub HE. Single Molecule Force Spectroscopy on Polysaccharides by Atomic Force Microscopy. *Science*. 1997; 275(5304):1295–7. Epub 1997/02/28. PMID: 9036852.
  53. Schwaiger I, Sattler C, Hostetter DR, Rief M. The myosin coiled-coil is a truly elastic protein structure. *Nat Mater*. 2002; 1(4):232–5. Epub 2003/03/06. <https://doi.org/10.1038/nmat776> PMID: 12618784.
  54. E AH, Heinz WF, Antonik MD, D'Costa NP, Nageswaran S, Schoenenberger CA, et al. Relative microelastic mapping of living cells by atomic force microscopy. *Biophys J*. 1998; 74(3):1564–78. Epub 1998/03/25. [https://doi.org/10.1016/S0006-3495\(98\)77868-3](https://doi.org/10.1016/S0006-3495(98)77868-3) PMID: 9512052; PubMed Central PMCID: PMCPCMC1299502.
  55. Rotsch C, Radmacher M. Mapping local electrostatic forces with the atomic force microscope. *Langmuir*. 1997; 13(10):2825–32. <https://doi.org/10.1021/la960874s> WOS:A1997WZ44700040.
  56. Sorci M, Dassa B, Liu H, Anand G, Dutta AK, Pietrovski S, et al. Oriented covalent immobilization of antibodies for measurement of intermolecular binding forces between zipper-like contact surfaces of

- split inteins. *Anal Chem.* 2013; 85(12):6080–8. Epub 2013/05/18. <https://doi.org/10.1021/ac400949t> PMID: 23679912; PubMed Central PMCID: PMC3760192.
57. Sauerbrey G. Verwendung Von Schwingquarzen Zur Wagung Dunner Schichten Und Zur Mikrowagung. *Z Phys.* 1959; 155(2):206–22. <https://doi.org/10.1007/Bf01337937> WOS:A1959WQ75600007.
  58. Voinova MV, Rodahl M, Jonson M, Kasemo B. Viscoelastic acoustic response of layered polymer films at fluid-solid interfaces: Continuum mechanics approach. *Phys Scripta.* 1999; 59(5):391–6. <https://doi.org/10.1238/Physica.Regular.059a00391> WOS:000080397800011.
  59. Mol NJd, Fischler MJE. *Surface plasmon resonance: methods and protocols.* New York: Humana Press; 2010. x, 286 p. p.
  60. Fischer M, Leech AP, Hubbard RE. Comparative assessment of different histidine-tags for immobilization of protein onto surface plasmon resonance sensorchips. *Anal Chem.* 2011; 83(5):1800–7. Epub 2011/02/15. <https://doi.org/10.1021/ac103168q> PMID: 21314134.
  61. Prime KL, Whitesides GM. Adsorption of Proteins onto Surfaces Containing End-Attached Oligo(Ethylene Oxide)—a Model System Using Self-Assembled Monolayers. *Journal of the American Chemical Society.* 1993; 115(23):10714–21. <https://doi.org/10.1021/ja00076a032> WOS:A1993MH75200032.
  62. Cho NJ, Frank CW, Kasemo B, Hook F. Quartz crystal microbalance with dissipation monitoring of supported lipid bilayers on various substrates. *Nat Protoc.* 2010; 5(6):1096–106. Epub 2010/06/12. <https://doi.org/10.1038/nprot.2010.65> PMID: 20539285.
  63. Tsai J, Taylor R, Chothia C, Gerstein M. The packing density in proteins: standard radii and volumes. *J Mol Biol.* 1999; 290(1):253–66. Epub 1999/07/02. <https://doi.org/10.1006/jmbi.1999.2829> PMID: 10388571.
  64. *Colloids and surfaces. B, Biointerfaces.* Amsterdam; New York: Elsevier; 1993. p. volumes.
  65. Voros J. The density and refractive index of adsorbing protein layers. *Biophys J.* 2004; 87(1):553–61. Epub 2004/07/09. <https://doi.org/10.1529/biophysj.103.030072> PMID: 15240488; PubMed Central PMCID: PMC3760192.
  66. Dutta AK, Belfort G. Adsorbed gels versus brushes: viscoelastic differences. *Langmuir.* 2007; 23(6):3088–94. Epub 2007/02/09. <https://doi.org/10.1021/la0624743> PMID: 17286418; PubMed Central PMCID: PMC3760192.
  67. Szeleifer I. Polymers and proteins: Interactions at interfaces. *Curr Opin Solid St M.* 1997; 2(3):337–44. [https://doi.org/10.1016/S1359-0286\(97\)80125-8](https://doi.org/10.1016/S1359-0286(97)80125-8) WOS:A1997XL16100012.
  68. Degennes PG. Conformations of Polymers Attached to an Interface. *Macromolecules.* 1980; 13(5):1069–75. <https://doi.org/10.1021/ma60077a009> WOS:A1980KM67900009.
  69. Bustamante C, Marko JF, Siggia ED, Smith S. Entropic elasticity of lambda-phage DNA. *Science.* 1994; 265(5178):1599–600. Epub 1994/09/09. PMID: 8079175.
  70. *American Chemical Society. Macromolecules.* Easton, Pa.: American Chemical Society. p. volumes.
  71. Grandbois M, Beyer M, Rief M, Clausen-Schaumann H, Gaub HE. How strong is a covalent bond? *Science.* 1999; 283(5408):1727–30. <https://doi.org/10.1126/science.283.5408.1727> WOS:000079102800049. PMID: 10073936
  72. Alber F, Dokudovskaya S, Veenhoff LM, Zhang W, Kipper J, Devos D, et al. The molecular architecture of the nuclear pore complex. *Nature.* 2007; 450(7170):695–701. Epub 2007/11/30. <https://doi.org/10.1038/nature06405> PMID: 18046406.
  73. Strawn LA, Shen T, Shulga N, Goldfarb DS, Wentz SR. Minimal nuclear pore complexes define FG repeat domains essential for transport. *Nat Cell Biol.* 2004; 6(3):197–206. Epub 2004/03/25. <https://doi.org/10.1038/ncb1097> PMID: 15039779.
  74. Kim SJ, Fernandez-Martinez J, Nudelman I, Shi Y, Zhang W, Raveh B, et al. Integrative structure and functional anatomy of a nuclear pore complex. *Nature.* 2018; 555(7697):475–82. Epub 2018/03/15. <https://doi.org/10.1038/nature26003> PMID: 29539637; PubMed Central PMCID: PMC6022767.
  75. *North American Membrane Society. Journal of membrane science. Membrane science and desalination.* Amsterdam,; Elsevier Scientific Pub. Co. p. volumes.
  76. *Desalination. 1976-: Membrane science and desalination.* Amsterdam,; Elsevier Scientific Pub. Co. p. volumes.
  77. Kusnezow W, Syagailo YV, Ruffer S, Klenin K, Sebald W, Hoheisel JD, et al. Kinetics of antigen binding to antibody microspots: strong limitation by mass transport to the surface. *Proteomics.* 2006; 6(3):794–803. Epub 2005/12/31. <https://doi.org/10.1002/pmic.200500149> PMID: 16385475.
  78. Frey S, Richter RP, Gorlich D. FG-rich repeats of nuclear pore proteins form a three-dimensional meshwork with hydrogel-like properties. *Science.* 2006; 314(5800):815–7. Epub 2006/11/04. <https://doi.org/10.1126/science.1132516> PMID: 17082456.

79. Weiss JN. The Hill equation revisited: uses and misuses. *FASEB J.* 1997; 11(11):835–41. Epub 1997/09/01. PMID: [9285481](#).
80. Gunawardena J. Models in biology: 'accurate descriptions of our pathetic thinking'. *BMC Biol.* 2014; 12:29. Epub 2014/06/03. <https://doi.org/10.1186/1741-7007-12-29> PMID: [24886484](#); PubMed Central PMCID: [PMCPMC4005397](#).
81. Mammen M, Choi SK, Whitesides GM. Polyvalent interactions in biological systems: Implications for design and use of multivalent ligands and inhibitors. *Angew Chem Int Edit.* 1998; 37(20):2755–94. WOS:000076892300001.
82. Raveh B, Karp JM, Sparks S, Dutta K, Rout MP, Sali A, et al. Slide-and-exchange mechanism for rapid and selective transport through the nuclear pore complex. *Proc Natl Acad Sci U S A.* 2016; 113(18):E2489–97. Epub 2016/04/20. <https://doi.org/10.1073/pnas.1522663113> PMID: [27091992](#); PubMed Central PMCID: [PMCPMC4983827](#).
83. Caspi Y, Zbaida D, Cohen H, Elbaum M. Synthetic mimic of selective transport through the nuclear pore complex. *Nano Lett.* 2008; 8(11):3728–34. Epub 2008/10/28. <https://doi.org/10.1021/nl801975q> PMID: [18950236](#).
84. Kowalczyk SW, Kapinos L, Blosser TR, Magalhaes T, van Nies P, Lim RY, et al. Single-molecule transport across an individual biomimetic nuclear pore complex. *Nat Nanotechnol.* 2011; 6(7):433–8. Epub 2011/06/21. <https://doi.org/10.1038/nnano.2011.88> PMID: [21685911](#).
85. Ananth AN, Mishra A, Frey S, Dwarkasing A, Versloot R, van der Giessen E, et al. Spatial structure of disordered proteins dictates conductance and selectivity in nuclear pore complex mimics. *Elife.* 2018;7. Epub 2018/02/15. <https://doi.org/10.7554/eLife.31510> PMID: [29442997](#); PubMed Central PMCID: [PMCPMC5826291](#).
86. Ketterer P, Ananth AN, Laman Trip DS, Mishra A, Bertolin E, Ganji M, et al. DNA origami scaffold for studying intrinsically disordered proteins of the nuclear pore complex. *Nat Commun.* 2018; 9(1):902. Epub 2018/03/04. <https://doi.org/10.1038/s41467-018-03313-w> PMID: [29500415](#); PubMed Central PMCID: [PMCPMC5834454](#).
87. Fisher PDE, Shen Q, Akpınar B, Davis LK, Chung KKH, Baddeley D, et al. A Programmable DNA Origami Platform for Organizing Intrinsically Disordered Nucleoporins within Nanopore Confinement. *ACS Nano.* 2018; 12(2):1508–18. Epub 2018/01/20. <https://doi.org/10.1021/acsnano.7b08044> PMID: [29350911](#); PubMed Central PMCID: [PMCPMC5834394](#).